Mesh Effects on Flow Solutions for a 2-D Multi-Element Airfoil Using Structured Overset Methods

Andrew M. Chuen*† and William M. Chan.‡
NASA Ames Research Center, M/S 258-2, Moffett Field, CA 94035

Current best-practices for mesh generation in a structured overset framework are evaluated to determine their effects on the accuracy and convergence of the flow solution on a two-dimensional sectional cut of the High-Lift Common Research Model (HLCRM) wing. Mesh parameters are varied independently and correlated with force and moment coefficients from the flow solutions to identify the trends and sensitivities of the parameter variations, and the characteristics of a best practice mesh. Grid convergence and mesh adaption studies are also performed to determine the minimum mesh quality needed in order for solution-based adaption to reach an accurate flow solution.

Nomenclature

C_p	=	pressure coefficient
C_l	=	lift coefficient
C_d	=	drag coefficient
$C_{d,p}$	=	pressure drag coefficient
$C_{d,v}$	=	viscous drag coefficient
c	=	chord
c_{ref}	=	reference chord length
n_{pTE}	=	number of points on trailing edge
$\Delta\theta_{LE}$	=	max turning angle per grid spacing at leading edge
Δs_{max}	=	global max spacing for near-body grids
Δs_w	=	normal wall spacing
Δs_{SL}	=	shear layer spacing
Δs_{wgTE}	=	wake-grid normal spacing at finite-thickness trailing edge
h_{SL}	=	shear layer region height
D_m	=	outer boundary distance of near-body mesh
$\vec{Q}$	=	conservative flow vector (density, momentum, internal energy)
q	=	individual element/flow variable of Q
R	=	distance from the center of the lift vortex

I. Introduction

A ‘‘good” quality mesh, in engineering applications, should balance the need for accuracy with the available computational resources. However, determination of mesh quality is difficult with no rigorous metrics. The a priori relationship between the accuracy of a solution and mesh inputs, aside from a truncation error analysis, is not easily discernible. While one can certainly perform a uniform mesh refinement to obtain a grid independent solution, this is rarely an optimal use of the available resources.

Best practices have been developed to facilitate the production of a good quality mesh. However, many best practices are based on heuristics as opposed to rigorous arguments. Consider, for example, the best practice of setting the leading-edge spacing to 0.1% of local chord [1]. While it does result in a reasonably fine spacing for most round leading edges in subsonic and transonic flow, it does not account for the local geometry and may not be sufficient for

*Pathways Student, Computational Aerosciences Branch, M/S 258-2, AIAA Student Member.
†Graduate Student Researcher, Univ. of California, Davis, Department of Mechanical and Aerospace Engineering.
‡Computer Scientist, Computational Aerosciences Branch, M/S 258-2, AIAA Senior Member.

leading-edges with extremely small radius of curvature. As such, it is necessary to examine these best practices and their sensitivities.

Another option is to utilize solution-based adaption. Use of adaption may reduce the requirements for a starting mesh to obtain a reasonably accurate solution. This, in turn, can reduce the turn-around time and the required expertise for mesh generation. However, solution-based adaption can still be impractical, expensive, or converge to the incorrect asymptotic solution [2][3]. It is especially costly if the flow solution is transient or oscillatory with dynamic flow features.

This paper seeks to evaluate the effects of mesh parameters in a structured overset grid framework for a two-dimensional (2-D) sectional cut of the High Lift Common Research Model (HLCRM). Additionally, this paper also seeks to determine the minimum mesh quality, based on the choice of such mesh parameters, needed in order for solution-based adaption to reach an accurate flow solution. A 2-D high-lift configuration is a viable configuration for experimenting with adaption as the flow features are relatively simple. It can serve as a testing ground before applying adaption to three-dimensional complex configurations.

The high-lift configuration consists of a slat, main, and flap element. The slat is deflected 30° and the flap is deflected 37°. Figure 1 shows the geometry of both the stowed and unstowed configuration. The local chord (c_{ref}) is

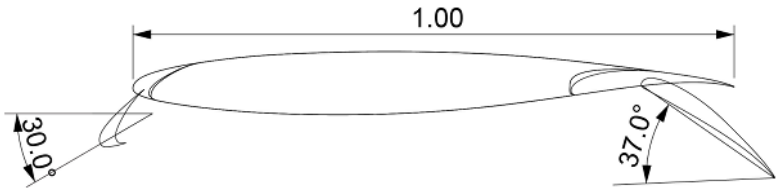

Fig. 1 High-lift configuration geometry [4].

1.00 m, and the global coordinate system is defined from the leading edge of the stowed configuration.

The study consists of two parts. First, a reference mesh is generated using the current best-practice parameters for overset structured mesh generation [5][6]. From there, each parameter is individually varied across a range of values to evaluate the effect on the solution and the configuration's lift curve and drag polar. A value is selected from each parameter to produce the best-practice mesh, which will be used to perform a grid convergence study. A secondary study on solution-based adaption is also performed to evaluate the ability to obtain a solution from a minimal-effort mesh. Table 1 shows the variables that define far-field flow conditions of the test case.

Table 1 Flow parameters for reference case.

Flow Parameter	M_∞	Re	α	γ	P_∞	T_∞
Value	0.2	5.0×10^6	8°	1.4	101 KPa	272.1K

Section II describes the methods and tools to build the overset meshes and compute flow solutions. Section III presents the reference mesh on which the parameter variation study will be carried out. Specific concerns are discussed on overset mesh hole-cutting, C verses O mesh treatment, and a priori flow knowledge. Section IV discusses the meshing study using parameter variation and solution adaption. Results of the study are presented in Sections V and VI. A summary is provided in Section VII.

II. Mesh Generation and Flow Computation

A. Mesh Generation Using Chimera Grid Tools

Chimera Grid Tools (CGT) is a suite of tools for pre- and post-processing CFD simulations using structured overset meshes [7]. It contains tools for geometry processing, surface mesh generation, and volume-mesh generation. These tools are accessible via a graphical user interface or the script library [8]. Additional tools are available for the assessment of grid quality, aerodynamic loads computation, and flow visualization.

The mesh generation procedure begins with geometry pre-processing. The initial geometry curves in the given IGES or STEP file are converted into a discrete representation. The slat and main elements are each prescribed by a set

of four curves, while the flap element is prescribed by three curves. For this geometry, Pointwise™is used to convert the file into a fine resolution PLOT3D file with 500 points per curve. Finite-thickness trailing-edge curves are defined using two points. Care is taken to ensure that regions of high curvature had a high concentration of points so that the curvatures are accurately captured in the final mesh.

Once the wall curves are in PLOT3D format, CGT scripts are used to generate the conformal meshes. First, the scripts are called to redistribute points on the surface geometry based on best practices. These curves are then used to generate the meshes using the hyperbolic mesh generation tool HYPGEN[9] in CGT. Specific details in the point redistribution and mesh generation are discussed in Section III.A.1. For these particular cases, only the near-body geometry-conforming grids and hole-cutting stencils are generated using CGT. Multi-layered off-body Cartesian meshes with successive levels of refinement are generated using OVERFLOW [10]. Domain connectivity is performed using X-ray hole-cutting. The far-field is extended approximately 1000 chords away in all directions.

B. Flow Computation Using OVERFLOW

OVERFLOW is a flow solver that solves the compressible Navier-Stokes equations on structured overset grids [10]. It also has the capability to generate off-body meshes and perform hole-cutting and grid connectivity through the domain connectivity function (DCF-XRAYS) [11].

To compute the flow, the HLLC scheme with Koren limiter is used to discretize the flux terms, and the SSOR algorithm with 10 subiterations is used to compute the implicit terms. While the reference case does not have shocks, the high end of the angle-of-attack sweep does exhibit a small supersonic bubble over the slat. The wall regions are set to viscous, adiabatic wall boundary conditions. Far-field boundary conditions are computed using Riemann-invariants. The Spalart-Allmaras (SA) model is used to model the turbulent effects.

OVERFLOW also has the ability to perform solution-based isotropic mesh adaption [12, 13]. The heuristic for adaption is based on the second undivided differences of the conservative flow variables,

$$S = \max_{i=j,k,l} \left\{ \max_{\vec{Q}} \left[\left(\frac{q_{i-1} - 2q_i + q_{i+1}}{2q_{ref}} \right)^2 \right] \right\}, \tag{1}$$

where q_{ref} is a reference quantity to normalize the difference. This sensor can identify both shocks and vortices [14].

Each solution is computed starting from free-stream flow. A solution is determined to be converged if all of the following conditions are met:

- Iterative relative residual errors drop five orders of magnitude
- C_l and C_m variations are below 10^{-4}
- C_d variations are below one-tenth of a drag count

For most of these cases, approximately 60000 iterations is needed to satisfy all of the convergence criteria. A typical case takes approximately one hour and twenty minutes to solve on twenty Intel IvyBridge CPUs.

C. Verification of SA Model in OVERFLOW

The OVERFLOW implementation of the SA model is verified with the 2D Airfoil Near-Wake with 500c Far-Field Extent test case [15]. The test case is computed on the meshes provided by the Langley Turbulence Modeling Resource (TMR) [16]. To run the cases on OVERFLOW, the airfoil-conformal grid is extended five points deep into the wake grid to ensure proper overlap for the numerical scheme described in the previous section. The overlap is point-matched to ensure the points are consistent with the original mesh.

Figure 2 shows the mesh convergence plots for the force coefficients. All solution are solved until the residuals drop by 10 orders of magnitude. In general, OVERFLOW shows good agreement with the reference results computed using CFL3D and FUN3D. Figure 3 also shows the mesh convergence of the minimum velocity in the near-wake at $x = 1.01$ and $x = 1.80$.

III. Baseline Mesh From Current Best-Practices

Table 2 shows the parameters that define the baseline mesh for the mesh parameter variation study. The mesh is based on the current best-practices in an engineering setting, which come from the medium mesh from prior Geometry and Mesh Generation Workshops [6]. This includes mesh parameters such as number of points on the trailing edge n_{pTE}, stretching ratio, max chord-wise spacing Δs_{max} on the wall surface, shear layer spacing Δs_{SL}, and shear layer

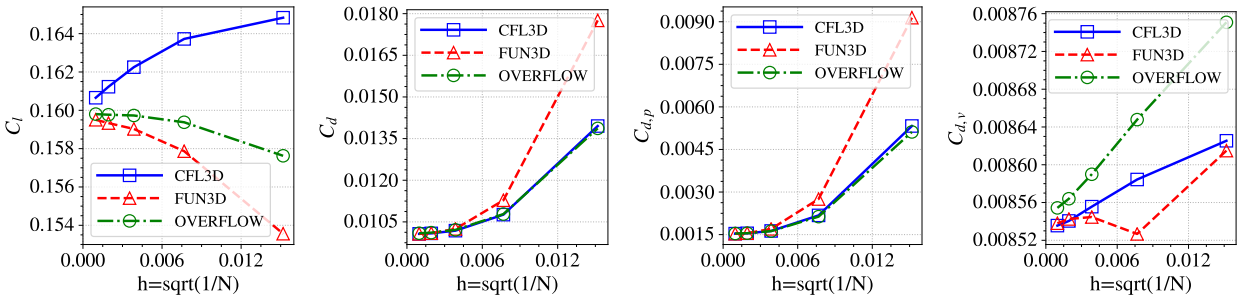

Fig. 2 Force convergence for (a) lift, (b) drag, (c) pressure drag , and (d) viscous drag.

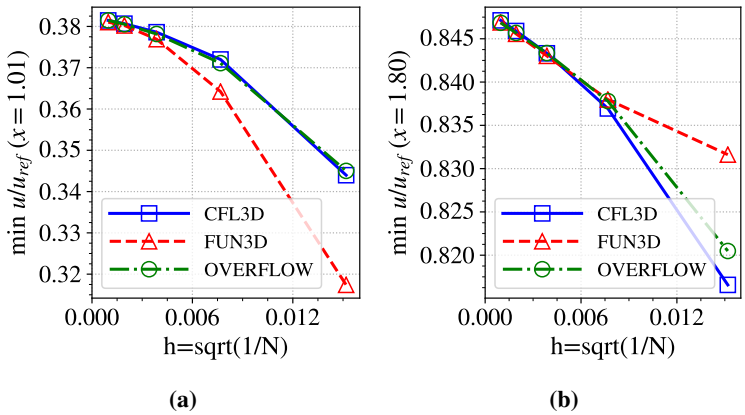

Fig. 3 (a) Velocity convergence in near-wake at $x = 1.01$ and (b) $x = 1.80$.

offset h_{SL} from the wall geometry. The shear layer spacing and shear layer offset height are parameters that control a band of uniform spacing for resolving the wake of an upstream element. The set max turning angle $\Delta\theta_{LE}$ for the leading edge spacing corresponds to a best-practice for a 0.1% of local chord mesh spacing at the leading edge. The wall spacing Δs_w, which is the first spacing normal to a wall in the mesh, is selected based on the freestream Reynolds number such that an estimated y^+ of approximately 1 is achieved at the wall.

The wake-grid spacing Δs_{wgTE} is a paramter that controls the wake grids added to the O meshes. This defines the spacing normal to the wake line at a finite-thickness trailing edge, which is further elaborated in Section III.A.2.

Table 2 Selected parameters for baseline mesh.

Mesh Parameter	**Value**
$\Delta\theta_{LE}$ (Leading-edge turning angle)	1.0°
n_{pTE} (Number of points on trailing edge)	9
Stretching Ratio	1.2
Δs_{max} (Max spacing on geometry surface)	$3.0\%c_{ref}$
Δs_w (Wall spacing)	4.323×10^{-6}m
Δs_{SL} (Shear-layer spacing)	$100\Delta s_w$
Δs_{wgTE} (Wake-grid spacing at finite-thickness trailing edge)	$5\Delta s_w$
h_{SL} (Shear-layer center offset)	~ 0.028m
Near-Body Mesh Topology	O-mesh
Far-Field Distance	$1000c_{ref}$

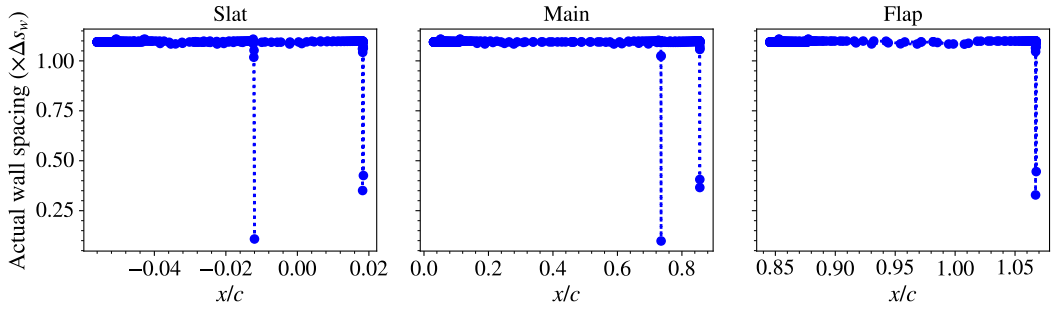

Fig. 4 Initial spacing normal to the wall.

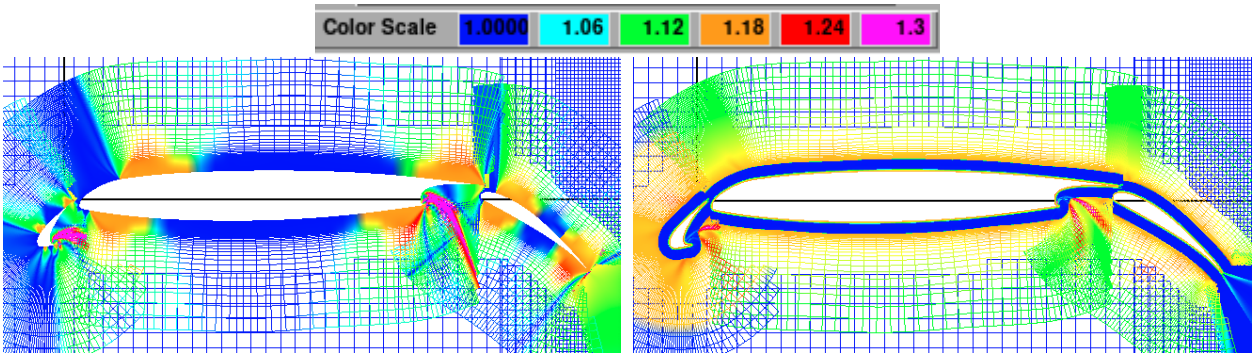

(a) **(b)**

Fig. 5 Stretching ratio of mesh in the (a) tangential and (b) normal directions.

Figure 4 shows the plot of the first grid spacing normal to the wall scaled by the length corresponding to a y^+ of 1. The plots show that the outputted first normal spacing generally satisfies the desired spacing of $y^+ \approx 1$. Figure 5 shows a plot of the stretching ratio in the tangential and normal directions. Overall, the grids show that the stretching satisfies the desired stretching ratio in the normal and tangential directions. The regions of extreme stretching in the tangential direction are due to the concavity in the cove regions and the local grid lines being forced together. The spacing close to the wall is largely unaffected.

A. Practices Specific to Overset Meshes

The success of the structured overset approach is made possible by the fact that the flow domain can be decomposed into multiple, structured, overlapping grids that can be generated independently of each other without needing to conform to other nearby grids or walls. Hole-cutting is then used to ensure that only points in the fluid domain participate in computing the solution. The grids must communicate through inter-grid interpolation with sufficient overlap while solving for the flow. At the minimum, the overlap region must span at least the stencil width of the flow solver.

A potential issue with overset grids is the possibility of solution "decoupling" across overlapping grids, which can occur when large gradients are present in an overlap region and the overlapping meshes differ in resolution. This results in each mesh capturing the flow solution at different resolutions, which can affect the overall accuracy of the solution. Meakin suggests interpolation should occur between cells of nearly the same size to ensure flow resolution compatibility between grids [17]. Excessive overlap can also cause this issue. Another strategy is to generally avoid placing overlapping regions at high-gradient locations, and to let a single grid dominate in the region [18]. These considerations are the motivating factors in the following best practices for generating overset meshes.

Table 3 Chord-wise locations (x/c) of leading edge spacing boundaries.

	Upper Surface	Lower Surface
Slat	-0.0506	-0.0426
Main	0.1124	0.0520
Flap	0.8773	0.8531

1. Grid Generation and Hole-Cutting Procedure

The near-body meshes that conform to the wall geometries are generated such that they extend a short distance away from the geometry surface. This can range from $0.089c_{ref}$ to $0.6c_{ref}$ depending on the choice of stretching ratio and max surface spacing. A background/off-body Cartesian mesh then connects the near-body meshes with the rest of the flow domain through hole-cutting and inter-grid interpolation.

Generating the conformal meshes starts with the surface discretization of the walls. The finite thickness trailing edges are discretized with a uniform spacing as defined by n_{pTE}, and the resulting spacing is used as an end spacing for the curves connected to the trailing edge. The leading edge is divided up such that each spacing does not exceed the specified max turning angle $\Delta\theta_{LE}$. Table 3 shows the locations on the upper and lower surfaces where the leading edge spacing is applied from the leading edge to the specified location. Leading edge spacing for the slat is applied to where the radius of curvature of the leading edge curve drops below 30% of the reference chord to ensure sufficient spacing in regions of high curvature. The main and flap elements, however, exhibited extended regions of leading edge spacing on the upper surface in anticipation of resolving flow features from upstream elements.

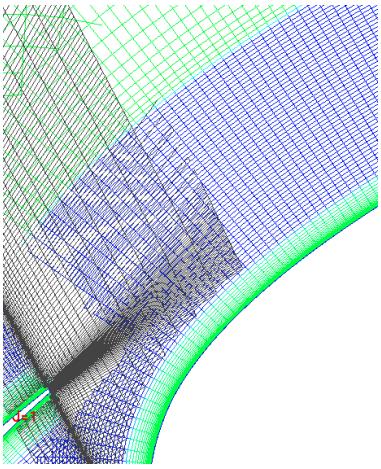

Fig. 6 Uniform spacing band (blue) in main element mesh for capturing slat wake.

At convex corners, such as the corner that joins the lower surface of the main element and the cove, the spacing at each leg is defined as a percentage of Δs_{max}. For the slat and cove, the spacing is defined as $0.5\%\Delta s_{max}$. The remaining surface curves are discretized with a stretched distribution as controlled by the stretching ratio and Δs_{max} parameters and maximum spacing placed in the middle of the curve.

Conformal grids are then generated from the resulting surface discretizations using hyperbolic methods. Each grid is grown starting from the wall spacing Δs_w with a one-sided stretched distribution until the normal spacing at the outer boundary reaches the max surface spacing Δs_{max}. For these meshes, only one layer of wall spacing is used. While two layers is generally preferred for numerical accuracy of the near-wall viscous effects in OVERFLOW [18], the main interest is in the resulting trends of the mesh parameter study instead of the actual values obtained. Additionally, it is expected that the variations will be largely attributed to pressure effects. Thus, the accuracy of the viscous will not have a significant effect on the observed trends.

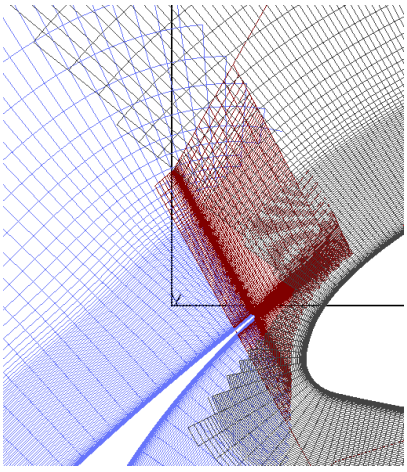

Fig. 7 Overlap between slat and main element meshes.

Because a wake is expected to develop off each element, the subsequent down-stream element mesh will include a band of uniform spacing in the normal direction. The center of this band is placed at an offset of h_{SL} away from the geometry, and the normal spacing is defined by Δs_{SL}. To incorporate this into the mesh, the mesh is grown with stretching from Δs_w to Δs_{SL}. The remaining distance from the current mesh outer boundary to h_{SL} is doubled and defines the thickness of the uniform band. The uniform band is generated, and then the remainder of the grid is generated as usual with stretching in the normal spacing.

Once the conformal meshes are generated, an off-body Cartesian mesh is generated such that the hyperbolic meshes are embedded in a uniform spacing region with edge-length of Δs_{max}. This ensures a smooth transition between the outer boundary of the near-body mesh and the background off-body mesh. The off-body mesh for this grid is generated using OVERFLOW.

For the high-lift configuration, grid overlap can be broken down into overlap between near and off-body meshes, and overlap between near-body meshes. The general best practice to obtain overlap between near and off-body meshes is to use DCF-XRAYS, which uses the surface definition with an offset based on the hyperbolic grid marching distance to define the cutting surface. However, for the two-dimensional case, it may be simple enough to define the cutting surface based on the n-th outer layer of the near-body mesh. This is preferable, since the hyperbolic marching distance

can vary greatly as the mesh parameters are varied in the study and a fixed percentage may not always guarantee sufficient overlap. For a stencil-width of 5 points, using the surface 8 grid-levels deep into the mesh from the outer boundary allows for sufficient overlap, especially for grid cells that are not perfectly aligned or similarly oriented.

The strategy for establishing the connectivity between near-body meshes is not as clear. In general, it is a good practice to avoid placing overlap in regions of large gradients. For example, adjacent near-body components must be cut such that the overlap occurs at the midpoint of the shortest distance between two bodies. Generally, this is achieved by using the geometry definition with an offset, and prevents overlap from occurring within the boundary layer region of either body. There are many possible approaches to perform the hole-cutting and domain connectivity that also satisfy this minimum requirement [19][20][21]. Thus, there also many possible variations of hole-cuts and domain connectivity for a given geometry.

For the sake of simplicity and consistency between the meshes, a manual hole-cutting approach using DCF-XRAYS is used instead. The approach begins with using the geometry offset to place the overlap at the midpoint of the shortest distance between two geometries. The process then continues with removing excessive overlap, especially where grids of each element extended too far into the grids of adjacent elements. The next step is to establish locations of where overlap and inter-grid communication should occur. There are natural locations to do this. One such region is the location between the trailing edge of one element (e.g. slat and main trailing edges) and the leading edge of the immediately aft element. Here, some of the cells exhibit similar alignment in the normal direction, which makes them ideal locations for overlap regions. Figure 7 shows the resulting mesh cutting and overlap region between the slat and main elements. Another such location is aft of the cove region in the bottom of the configuration. Care is taken to not place the overlap too close to the cove regions to avoid having the overlap protrude into the shear layer. Figure 8a shows an example mesh with the resulting hole-cut between near-body meshes. This approach allows the overlap between the meshes occur at the same locations as the mesh is changes in the parameter study.

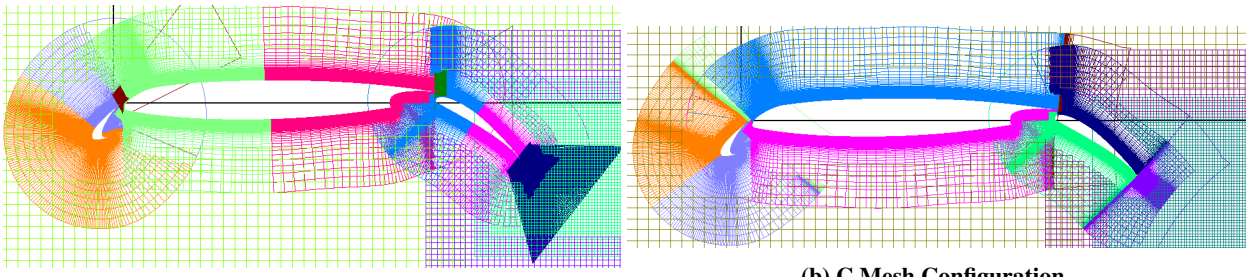

(a) O Mesh Configuration.

(b) C Mesh Configuration.

Fig. 8 Meshes generated for each mesh toplogy type in a structured-overset mesh framework.

2. O vs. C Mesh

When generating a structured mesh for an airfoil, the user must make a choice between using a C or O mesh topology. For flow around a single airfoil, it may be prudent to use a C mesh with natural clustering normal to the extrapolated trailing edge direction. However, this presumes that the direction of the wake is known a priori. If the flow separates or the wake develops in a different direction, the clustering is not beneficial. Excessive clustering far away from the airfoil surface also introduces convergence issues. "Fanning out" the wake can mitigate these issues, but this depends on the capabilities of the mesh generation software. Additionally, in the case of OVERFLOW, the boundary condition along the C grid's wake line is an explicit update, which can further exacerbate the convergence problem.

On the other hand, an O mesh does not have ideal clustering in the wake like the C mesh does. However, in an overset framework, an O mesh can achieve a similar resolution by adding a wake grid. The wake grid also offers greater control of the fanning since the grid is generated separately from the O mesh. With the addition of the wake grid, the O mesh should be able to produce results that are comparable to the C mesh. To verify this, the reference case is computed using a grid with an O mesh topology and another grid with a C mesh topology.

The C mesh grid is generated in a similar fashion to the O-mesh, except the starting wall curve includes a wake-line normal to the trailing edge. The wake line exhibits a stretched distribution of grid points, where the near-wall spacing is the grid spacing at the finite-thickness trailing edge, and the far-end spacing is Δs_{max}. The length of the wake line is defined to be the predicted normal marching distance when generated using hyperbolic grid generation. The grid is then

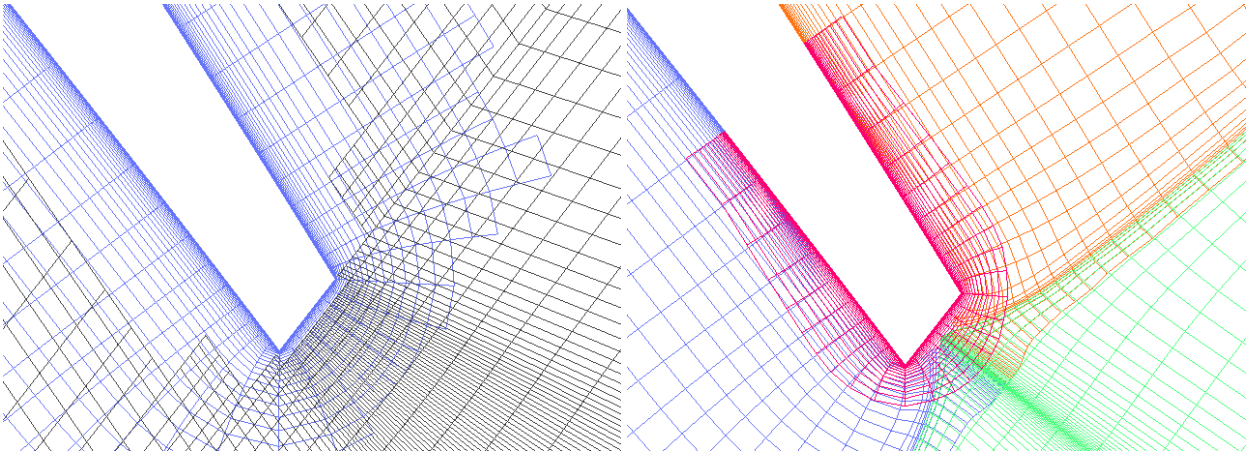

(a) O Mesh . **(b) C Mesh.**

Fig. 9 Mesh overlap in flap trailing edge for O mesh and C mesh.

grown hyperbolically like the O-mesh. However, variable normal spacing is used in the wake. The points at the trailing edge start at viscous wall spacing, while the points at the far end start with Δs_{SL}, with linear variation in between. The grid at the trailing edge grows normally, while the grid at the far end grows with constant spacing, until all normal spacing reaches Δs_{SL}. At this point, the mesh is generated normally with the growth of the shear-layer region and the rest of the volume mesh. The final grid exhibits a slight fanning due to the constant spacing at the far end of the wake.

To avoid the issue of the explicit update along the wake line, the C mesh is split into three grids with an OVERFLOW tool called *Ctop2*. This combines the wake region into a single grid, and splits the grid on the geometry surface into upper and lower grids. Finally, to improve the viscous resolution at the finite-thickness trailing edge, a small cap grid is added to ensure wall spacing at the trailing edge.

Table 4 Force and moment coefficient comparison of solutions computed using O and C meshes.

	O Mesh	C Mesh	Diff ($\times 10^4$)
Total C_l	3.22486	3.22499	1.23
Total C_d	0.04002	0.03960	-4.22
Total C_m	-0.52188	-0.52175	1.27
Slat C_l	0.28456	0.28486	2.96
Slat C_d	-0.28522	-0.28567	-4.53
Slat C_m	0.08262	0.08271	0.90
Main C_l	2.51266	2.51238	-2.77
Main C_d	0.03906	0.03915	0.95
Main C_m	-0.28350	-0.28339	1.09
Flap C_l	0.42765	0.42775	1.03
Flap C_d	0.28617	0.28611	-0.64
Flap C_m	-0.32100	-0.32107	-0.72

The wake grid for the O mesh is constructed such that it resembles the wake of the C mesh. At the trailing edge, a line tangent to the trailing edge is defined from the center of the trailing edge to an end point with a distance of approximately 2.5 times the expected shear-layer thickness. The point distribution exhibits a mix of uniform and stretched distributions

to mimic the normal growth of the volume mesh with shear layer resolution. At the trailing edge, however, a uniform spacing is used. The C mesh in this region typically has wall normal spacing. For the O mesh wake grid, however, a uniform spacing of $\Delta s_{wgTE} = 5\Delta s_w$ provides comparable resolution for the region. A second curve at the far end of the wake-line is defined with a length of twice the hyperbolic marching distance and uniform spacing. The two curves are combined to form a mesh using transfinite interpolation, and the spacing is redistributed like that of the C mesh. An additional rectangular grid is added forward of the first curve to improve connectivity between the O mesh and the wake grid. The majority of the O mesh past the trailing edge is entirely cut except for the necessary overlap at the boundaries of the wake grid, and the forward grid is cut to extend into the geometry. Figure 8 shows the resulting O and C meshes, and Figure 9 shows the resulting trailing edge configurations for both the O and C mesh topologies.

Table 4 shows the resulting force and moment coefficients computed with each mesh. While solutions for airfoils computed solely with O or C meshes can differ by 5%[5], the results show that the discrepancy between the two solutions can be reduced to a few counts with the addition of a wake grid. While this is insufficient to demonstrate equality of the solutions, it does demonstrate that an approach can be taken to reduce the difference in the solutions between the two grids.

B. A Priori Knowledge of the Flow

As discussed earlier, a band of uniform normal spacing is added to the main and flap elements to capture the wake from an upstream element. Rogers showed that it is necessary to refine the mesh at the shear layer to ensure that the correct drag from the momentum loss is obtained [22]. The uniform band of spacing is also applied to the slat to refine the cove region and improve the resolution of the shear layer in the cove.

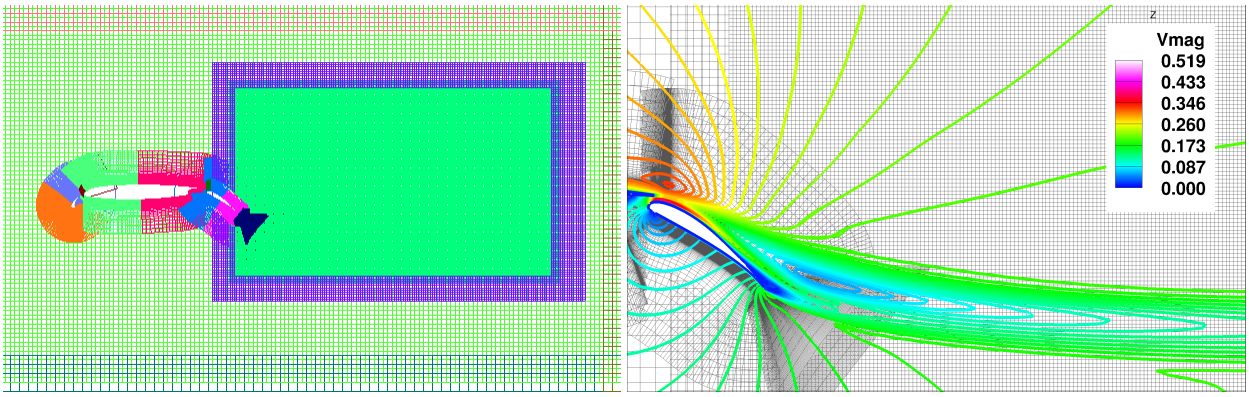

(a) **(b)**

Fig. 10 (a) Added wake block (lime green and purple) and (b) resolved wake aft of the flap element.

For this particular configuration and angle of attack, the wake of the main-element decelerates aft of the flap element. This feature is also convected downstream with the flow aft of the flap separation to combine into a single wake. Some initial computations revealed that the solution is sensitive to the resolution of this flow phenomenon. A refinement block is added to the baseline mesh and refines the wake region downstream of the geometry configuration. Since the baseline mesh corresponds to a mesh with medium fineness, the refinement block has a grid spacing of $0.25\Delta s_{max}$ to ensure that there are approximately twenty points across thickness of the wake. Figure 10 shows the refinement block added to the baseline mesh and the increased resolution of the wake in the velocity magnitude.

A small experiment was conducted to examine the effect of the length of the resolved wake. Off-body adaption is utilized to resolve the wake up to 1, 2, 5, 10, 20, 50, and 100 chords downstream of the configuration. Figure 11 and 12 show the lift and drag coefficients, respectively, as they vary with the downstream wake resolution distance. After approximately 10 chords downstream, the solution appears to shows reduced sensitivity to the downstream length refined wake. The solutions show much greater variance between resolving one and two chords downstream than between two and 100 chords downstream, indicating that a block length below two chords may be insufficient to resolve the wake. On the other hand, resolving the wake at distances beyond a few chords downstream using manually-generated meshes can be impractical without in-depth a priori knowledge of the flow or mesh adaption capabilities. Based on the available information for the $\alpha = 8^\circ$ reference case, the baseline mesh utilizes a wake block with a downstream length of two

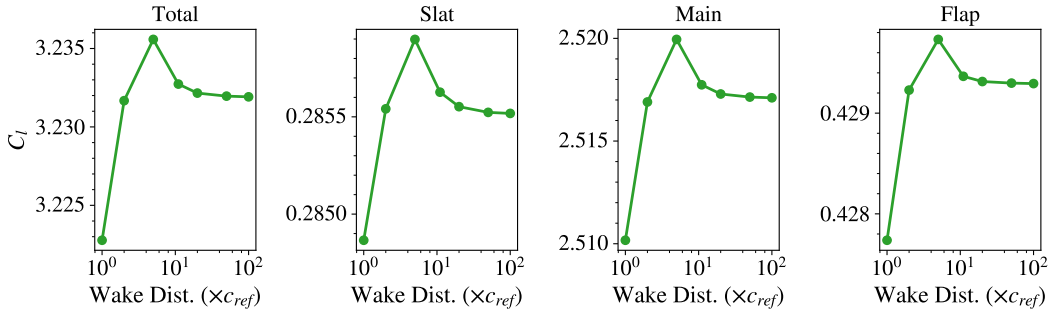

Fig. 11 Lift coefficient trends with wake refinement block length.

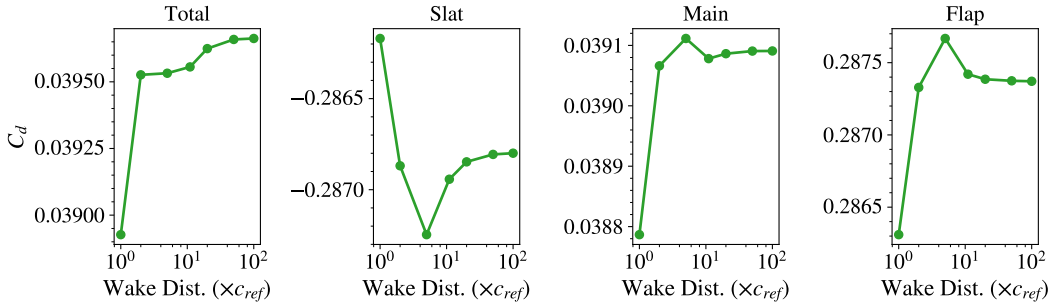

Fig. 12 Drag coefficient trends with wake refinement block length.

chords. That is not to say that two chords is necessarily the best practice. Other considerations, such as the validity of turbulent wakes in two dimensions and a lack of a reference solution based on experiment, add to the difficulty of selecting a reasonable length.

IV. Mesh-Effect Study Overview

A. Meshing Parameter Study

The mesh parameters of interest in this study are the trailing edge resolution, maximum turning angle of the leading edge spacing, maximum stretching ratio, global maximum surface spacing, and shear-layer spacing. Instead of varying a uniform fixed spacing at the leading edge, varying the maximum turning angle at the leading edge is chosen to be more general in consideration of the curvature of the geometry. Table 5 details the particular values of each parameter chosen, and how they are varied in the study. These parameters are chosen because of their direct influence on how the mesh is generated close to the body. Note that these parameters are varied in the same manner across all three elements. For example, for the case of $n_{pTE} = 11$, all elements exhibit a trailing edge discretized by 11 points. An alpha-sweep is also examined for each parameter variation with the same ambient conditions. The alpha-sweep is computed for every two degrees from $-2°$ to $26°$.

Table 5 Variable ranges for parameter study (reference parameters bolded).

Mesh Parameter	Values
n_{pTE}	3, 5, **9**, 11, 17
$\Delta\theta_{LE}$	0.125°, 0.25°, 0.5°, **1.0**°, 2.0°
Stretching Ratio	1.05, 1.1, 1.15, **1.2**, 1.3, 1.4
Δs_{max} (% of c_{ref})	1.0%, 1.33%, 2.0%, **3.0%**, 4.5%
Δs_{SL} ($\alpha \times \Delta s_w$)	25, 50, **100**, 200, 400

Based on the examined results, we will determine a best-practice mesh. This mesh is then utilized in a grid-convergence study, where each mesh parameter directly associated with a mesh spacing is successively halved, and a finer mesh is generated. The first layer of wall spacing (determined by the Reynolds number), however, is held fixed through the refinement levels. Because the velocity profile u^+ varies linearly with y^+ when $y^+ < 5$, an initial spacing of $y^+ = 1$ is sufficient to resolve the linear behavior. Refining the wall spacing does not improve the resolution of flow features, and only increases the stiffness of the system due to the extremely small local spacing.

B. Adaption Study

This part of the study will examine how well adaption can improve the accuracy assuming the user has no a priori knowledge of mesh-generation best-practices and physics of the flow. The study will start with a mesh on the coarse end of the parameter spectrum from Table 5, seeking the minimum mesh quality needed to achieve an accurate solution via adaption. Different levels of refinement will also be investigated to determine its effect on the solution.

V. Meshing Parameters Study Results

A. Variation of Trailing-Edge Resolution

Table 6 shows the node count changes as the trailing edge resolution changes. The grid growth is relatively mild, since only the resolutions at the trailing edge and one grid-spacing at the end of each curve connected to the trailing edge are changed. Figure 13 shows the pressure and skin-friction coefficients for each different trailing edge resolution. The discrepancies in the pressure coefficients occur mostly on the upper surface near the trailing edge of the slat element. The lower pressures on the upper surface for the finer solutions indicate the flow is faster in that region. However, in

Table 6 Node count with variations in trailing edge resolution.

$\mathbf{n_{pTE}}$	3	5	9	11	17	21
Node Count	222625	227005	231795	234535	238553	241173

the main and flap elements, the coarser resolutions have a lower pressure, especially in the suction peak. This seems to indicate that the resolution of the trailing edge affects the momentum of the immediate downstream element. It is possible that the increased resolution introduces more momentum loss into the flow over the downstream element, which appears to reduce the the circulation in the solution. In addition, increasing the resolution also causes the inflection point where the separation occurs on the flap to occur further upstream.

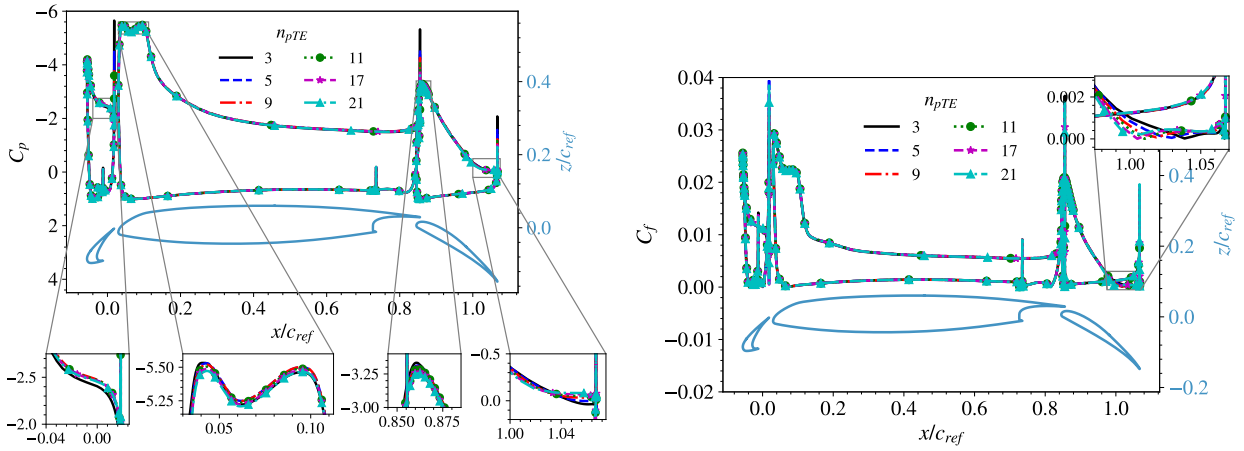

(a) **(b)**

Fig. 13 (a) Section pressure and (b) skin-friction coefficients for variations in trailing edge resolution.

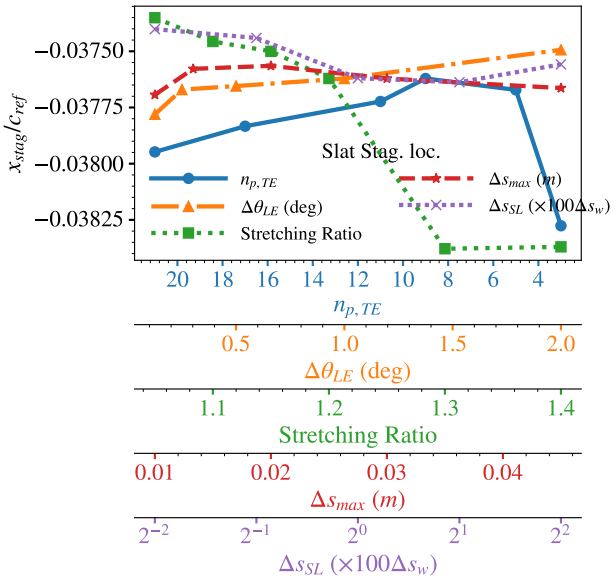

(a) Slat stagnation point.

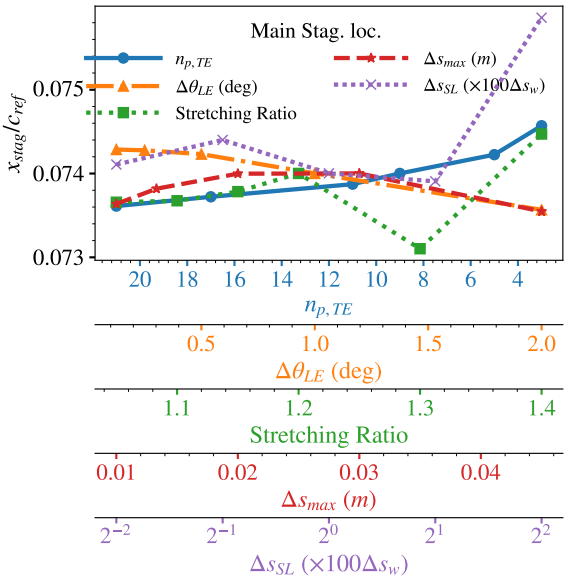

(b) Main stagnation point.

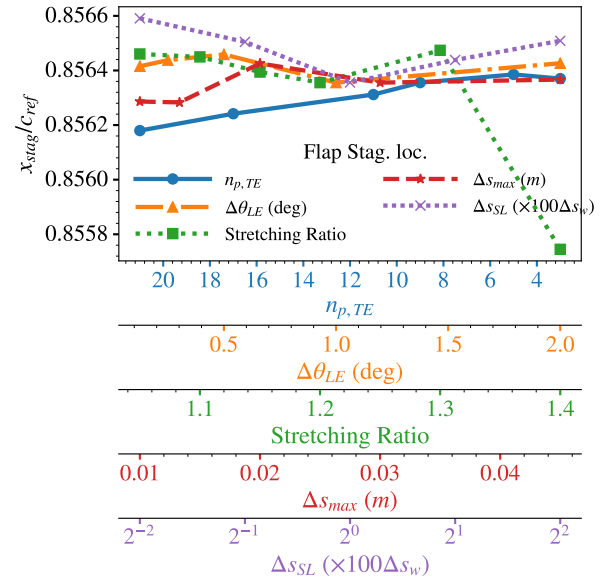

(c) Flap stagnation point.

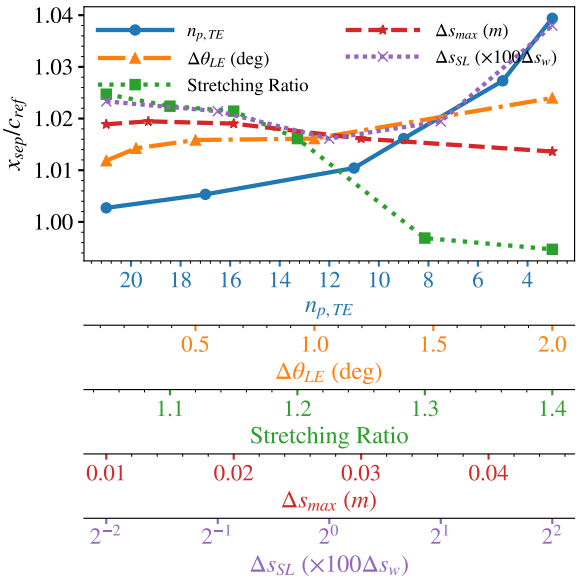

(d) Flap separation point.

Fig. 14 Stagnation and separation point locations for variations in the mesh parameters.

The skin-friction distribution also shows some discrepancies between the solutions. The lowest resolutions show a significantly delayed separation in comparison to the finer resolutions. It is important to note that the trailing-edge spacing is used as an end spacing for the upper and lower surfaces of each element, and its fineness drives the adjacent fineness of the surface curves. The coarse resolutions were likely unable to resolve the important flow phenomena. Additionally, it is also likely that three points is insufficient to capture the effect of the momentum loss of the wake for a finite-thickness trailing edge.

The stagnation points show subtle changes relative to the variation in trailing edge resolution. Figure 14 shows the variation of the stagnation and separation points on each element as it varies with each parameter. The range of variations of the stagnation points in each element is less than 0.1% of the chord. Generally, each element exhibits a

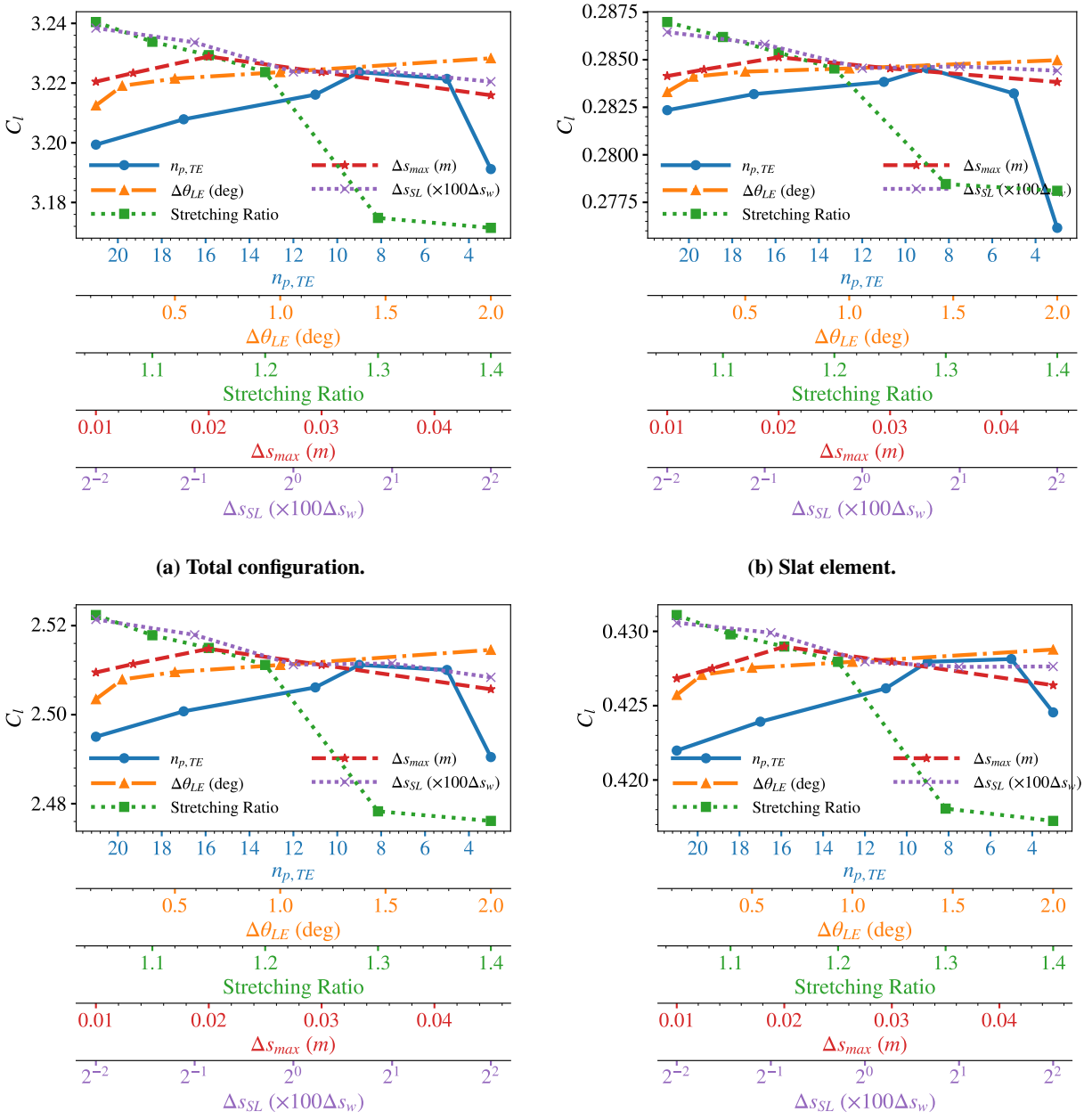

(a) Total configuration. **(b) Slat element.**

(c) Main element. **(d) Flap element.**

Fig. 15 Lift coefficients for variations in the mesh parameters.

forward traversal of the stagnation points as the resolution increases, indicating a reduction in the circulation related to the lift.

Similar to what is observed in Figure 13b, the separation points in Figure 14d, show dramatic variation with the trailing edge resolution. The range of separation point locations cover nearly 4% of the reference chord. Again, this change in the separation point with the trailing-edge resolution is likely due to the resolution of the wake developed off the finite thickness trailing edge. The wake captures the momentum loss in the flow, which makes the flow less resistant to the adverse pressure gradient further downstream. Increasing the resolution is likely capturing more of the dissipation associated with the momentum loss in the wake. It is interesting to observe that the separation point appears to exhibit monotonic convergence as it varies with the trailing edge resolution, indicating that the solution may reach a

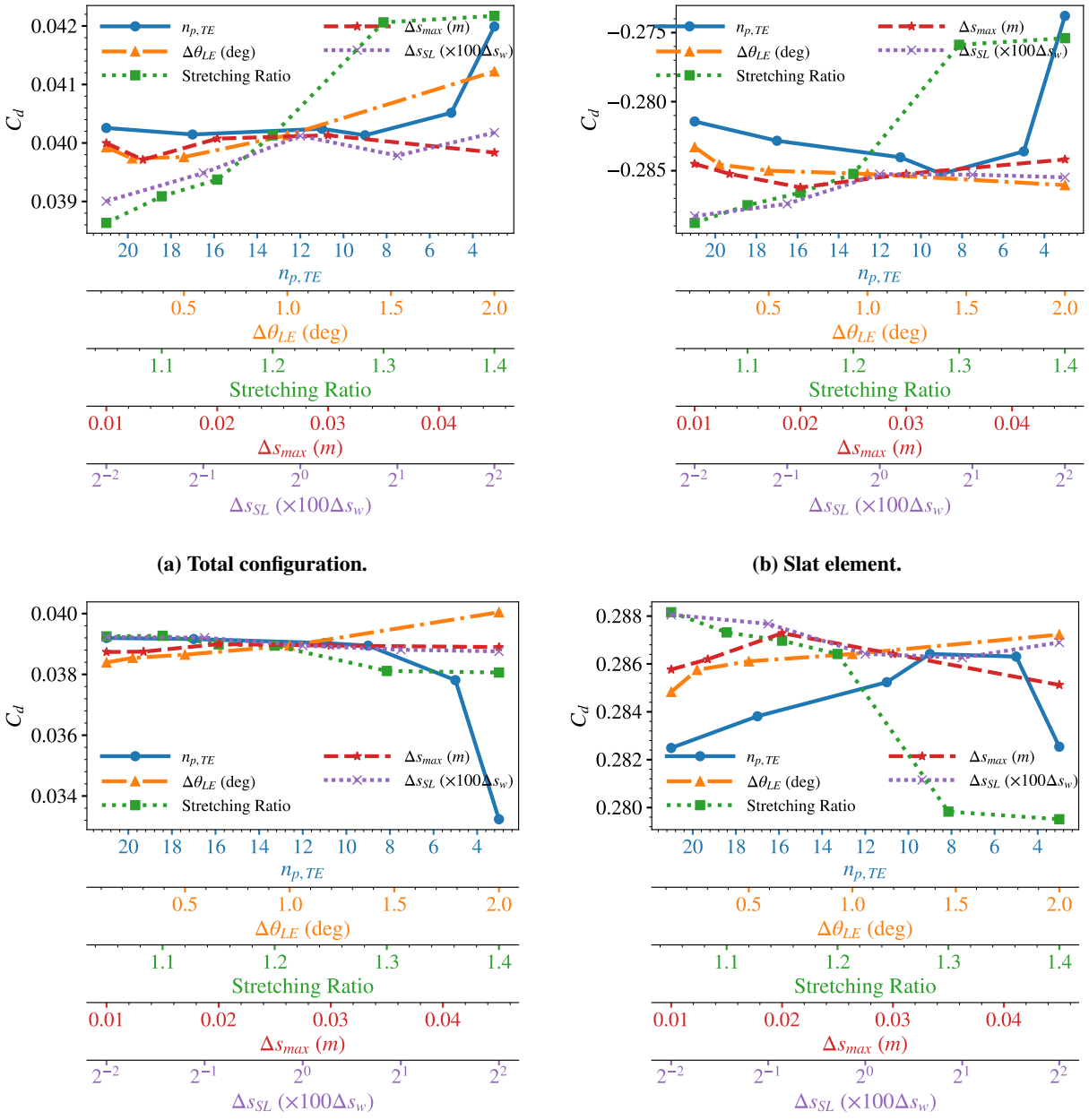

(a) Total configuration. **(b) Slat element.**

(c) Main element. **(d) Flap element.**

Fig. 16 Drag coefficients for variations in the mesh parameters.

point where it is independent of the variations in the trailing edge resolution.

Figure 15 shows the lift coefficients of the total configuration and each element as they vary with the trailing edge resolution. There is an approximate range of 300 lift count variation in the full configuration. Much of the variations occurs in the main element, which exhibits a 200 count variation in lift. The other elements only vary on the order of tens of counts. On the other hand, the drag shows the opposite situation in Figure 16. The total drag only varies on the order of counts with the exception of the coarsest solution. The main element also exhibits a similar result. The slat and flap elements, however, exhibit variations on the order of tens of counts with the exception of the large variation in the slat drag for the coarsest solution. Interestingly, however, the moment coefficients in Figure 17 only vary in the tens of counts in the full configuration and also for each element.

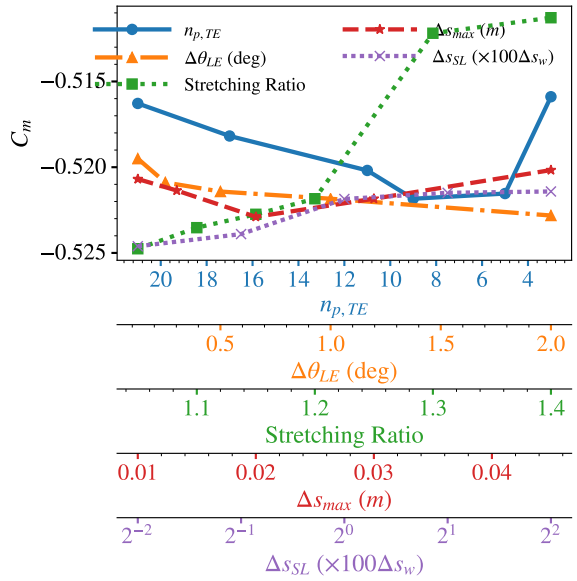

(a) Total configuration.

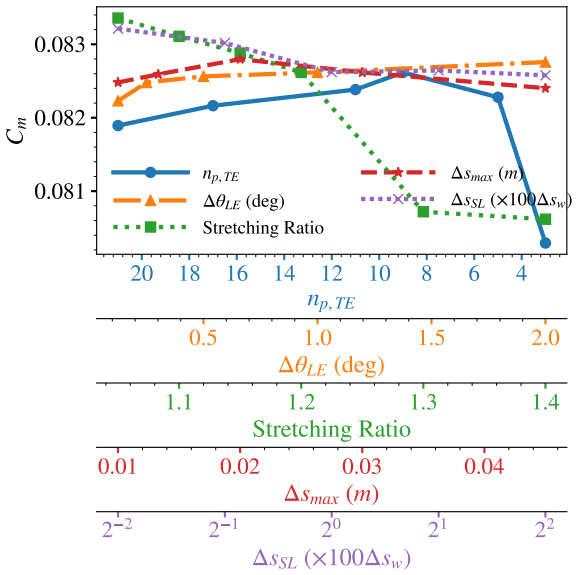

(b) Slat element.

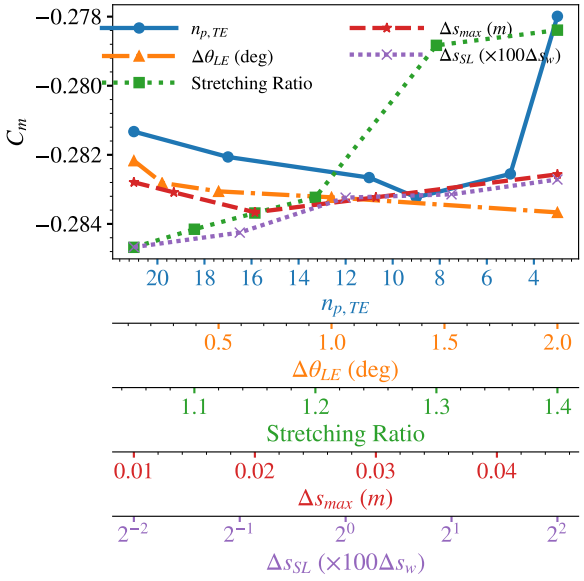

(c) Main element.

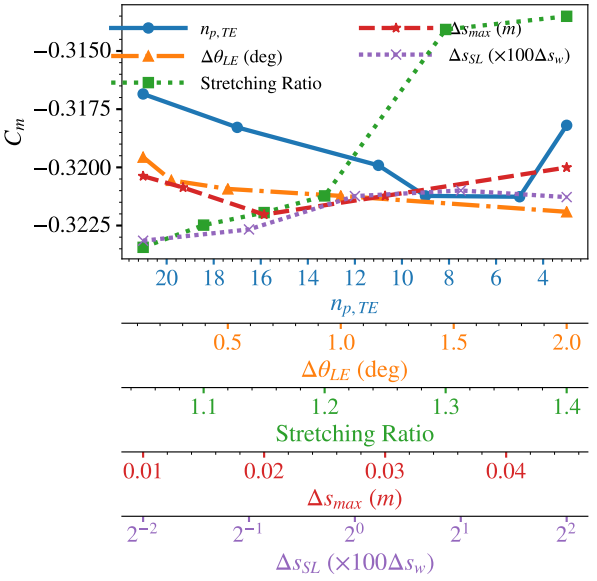

(d) Flap element.

Fig. 17 Moment coefficients for variations in the mesh parameters.

Figure 18 and 19 shows the breakdown of the drag into pressure and viscous drag components. Figure 18 shows the variation of the pressure drag, and the variations are similar to that of the full drag shown in Figure 16. Figure 19 shows the variations of the viscous drag. The fact that the total variations are less than a full drag count in range indicates that the viscous drag is mostly nonsensitive to the variation in the trailing edge resolution.

The range of variations in the lift are approximately 1-2% of the integrated coefficients, which can explain the slight differences in the pressure coefficients. It is interesting to note that, despite the reduced resolution of the viscous dissipation in the trailing edge wake, the drag increases and the lift decreases for a coarser trailing edge resolution. This is especially the case for the slat element. The drop in lift and increase in drag indicates that the effect of pressure on the drag has increased, which, for most airfoil configurations, occurs when the circulation due to the lift has decreased. The

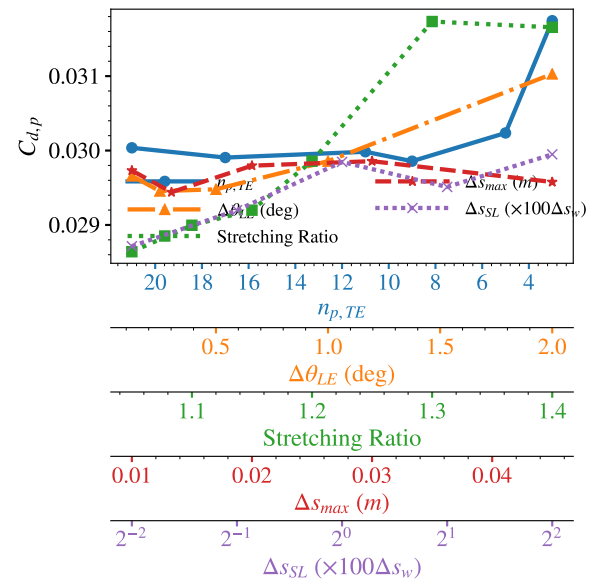

(a) Total configuration.

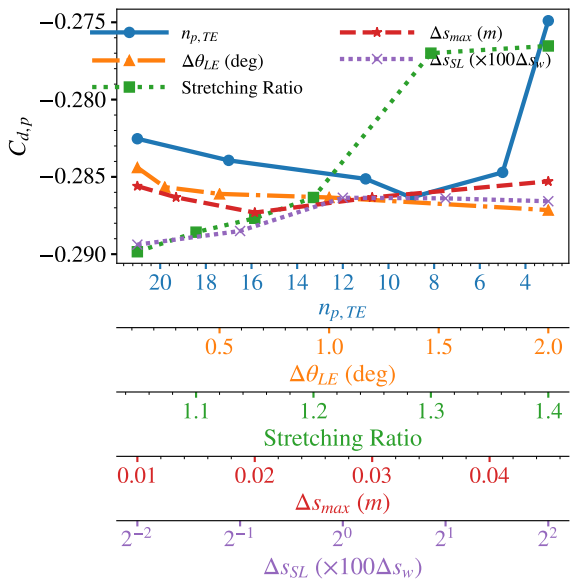

(b) Slat element.

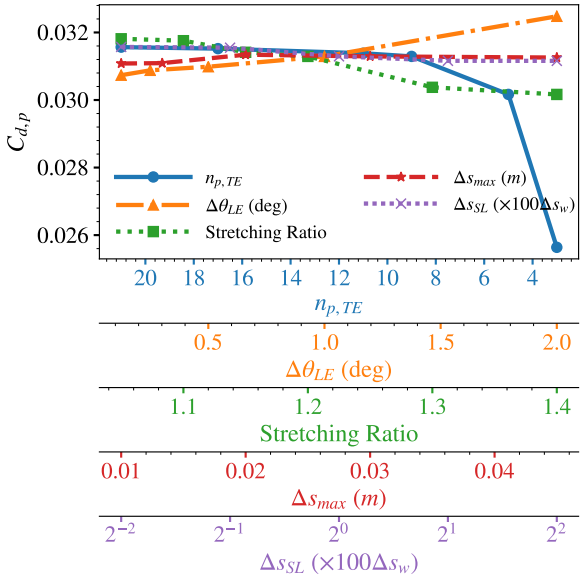

(c) Main element.

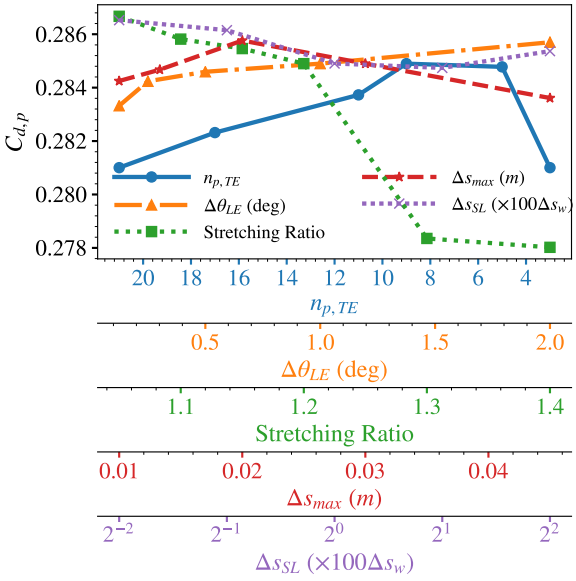

(d) Flap element.

Fig. 18 Pressure drag coefficients for variations in the mesh parameters.

discrepancy occurring near the trailing edge of the slat also indicates to this, since this is the flow right at the suction peak. Additionally, the zoom in Figure 13a indicates the pressure just upstream of the suction peak is slightly higher pressure for the coarsest distribution. This seems to indicate that trailing edge resolution has some effect on the ability of the mesh to accurately capture the suction peak, and thus the effect of the circulation on the solution.

Figure 20a and 20b shows the lift curve and drag polar for the full configuration. While the resolution and discrepancies are not as finely shown as the other plots, it can still be observed that the coarsest resolutions, three and five points, exhibit the largest discrepancies with the other solutions. At the lift peak, the coarsest resolutions are unable to capture the $C_{l,max}$. In the case of the drag polar, the reduced lift also comes with increased drag. The discrepancies between the resolutions are harder to distinguish past nine points on the trailing edge, indicating that nine

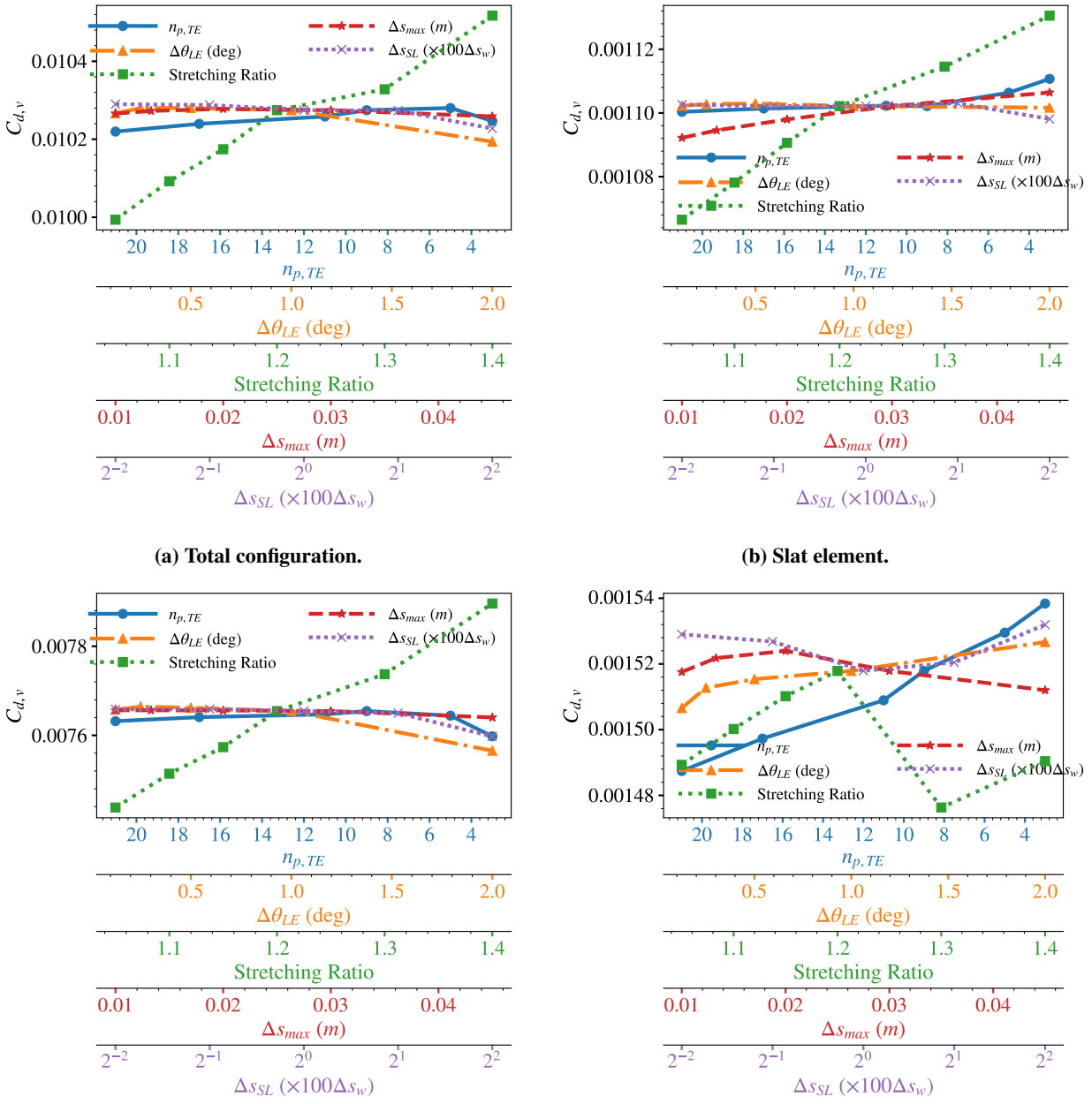

(a) Total configuration.

(b) Slat element.

(c) Main element.

(d) Flap element.

Fig. 19 Viscous drag coefficients for variations in the mesh parameters.

points is a reasonable minimum resolution to capture the relevant physical phenomena. The solutions also exhibit less discrepancies in the linear regions of the lift curve.

B. Variation of Max Leading Edge Turning Angle

Table 7 shows the point growth as the max turning angle around the leading edge is changed. Like the trailing edge resolution, the point growth is relatively minimal since it is localized in the leading edge portion of each grid. An increase in resolution by a factor of 16 from the coarsest setting only resulted in an increase in the point count by approximately a factor of two.

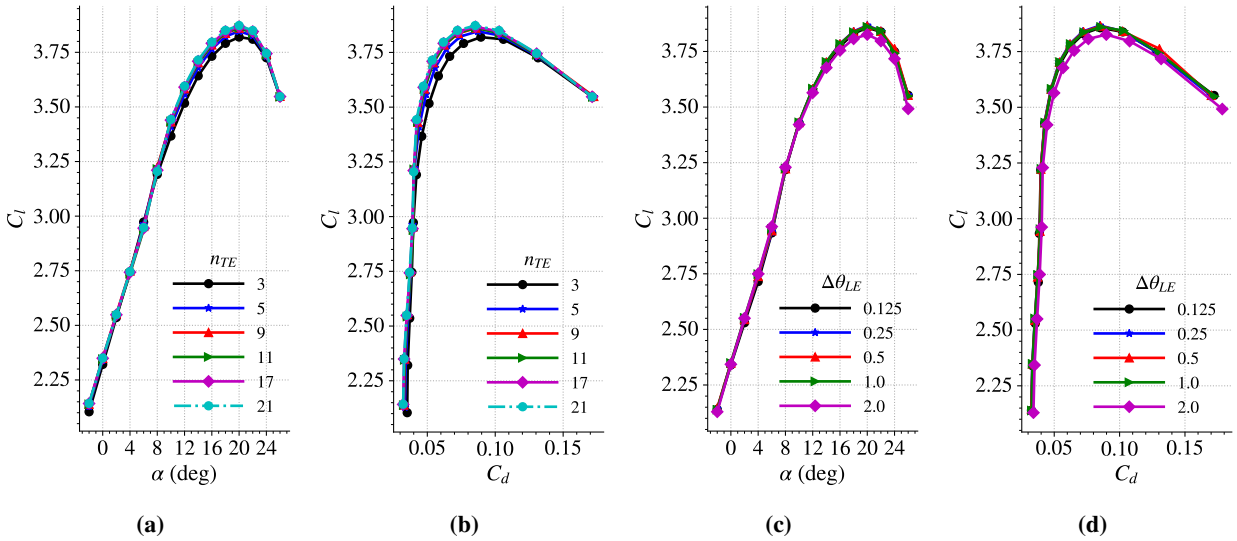

Fig. 20 Lift and drag polars for variations in trailing edge resolution ((a) and (b)) and leading edge resolution ((c) and (d)).

Figure 21 shows the pressure and skin-friction coefficients for variations in the max turning angle at the leading edge. Slight differences are present in the pressure and skin-friction coefficients as the solution changes with the leading-edge refinement. The pressure coefficient distribution exhibits variations over the upper surface of the slat. There are also slight changes in the skin-friction coefficient due to the variations in the separation point.

Table 7 Node count with variations in max leading edge turning angle.

$\Delta\theta_{\mathbf{LE}}$	0.125°	0.25°	0.5°	1.0°	2.0°
Node Count	527803	359971	275551	231795	208041

Like the coefficient distributions, associated slight changes are also present in the locations of the stagnation and separation points. Figure 14 only shows a max variation range of around $0.01\%c_{ref}$ for the stagnation points, and Figure 14d shows a variation range of around $1\%c_{ref}$ for the separation point. The traversal of the separation point can potentially be attributed to momentum loss from the increased tangential resolution of the wall.

Figure 15 shows that the lift varies over a range of 150 counts as the spacing is varied. The largest contributor to this range appears to come from the main element in Figure 15c, while Figures 15b and 15d show that the slat and flap only vary approximately twenty counts each. This is a variation range of approximately 0.7% and 0.4% for the slat and flap, respectively, while the main element has a range of approximately 0.6%. Overall the lift appears to decrease as the resolution is increased. The drag also exhibits similar behavior. Figure 16 shows that the drag also decreases with the leading edge spacing for the full configuration and main and flap elements. The exception is the slat drag in Figure 16b, which shows the drag increasing as the spacing is decreased. All elements vary on the order of a few tens of counts. The moment coefficient also exhibits a similar variation pattern in Figure 17.

Further examination of the drag breakdown in Figure 18 and 19 reveals that the majority of the drag variation comes from the pressure drag contribution. The cause of this phenomenon is likely due to the increased resolution in the suction peak regions of each element. Typically, improving the resolution of an under-resolved suction-peak region on an airfoil can increase lift and reduce drag due to improved capturing of the acceleration. However, the suction peak of the main and flap element have a shear layer intersecting through the region. Thus, increasing the resolution may not change the solution in the expected manner. It is possible that the increased resolution did reduce the drag as expected because of the resulting surface pressures. The decrease in lift, however, can potentially be attributed to the presence of the shear layer in the suction peak affecting the resulting circulation.

Figure 20c and 20d show the lift and drag polars of the configuration as it varies with the leading edge spacing. The results indicate that the finer settings exhibit small variations from the reference mesh, and that only the coarsest value

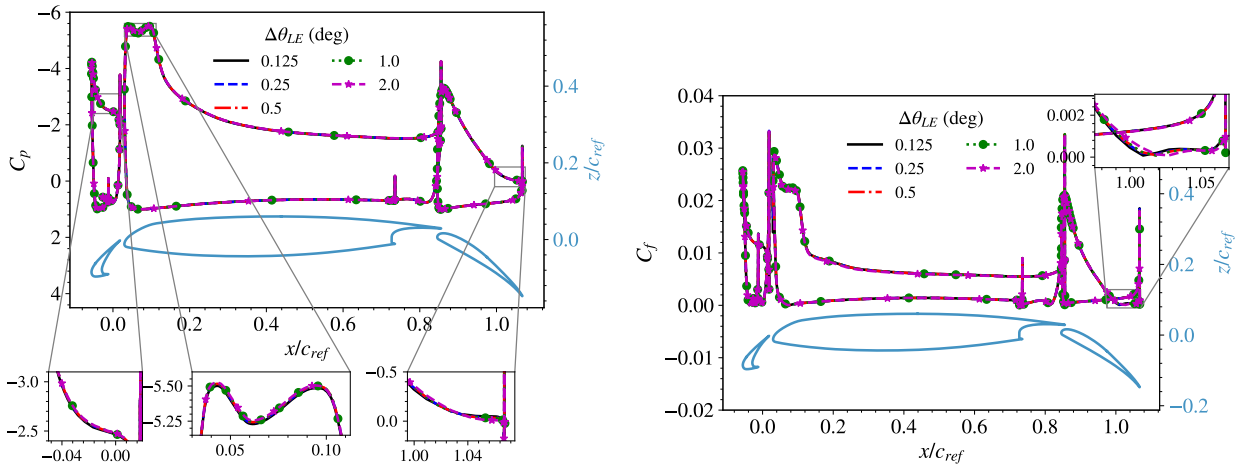

(a) **(b)**

Fig. 21 (a) Section pressure and (b) skin-friction coefficients for variations in max leading edge turning angle.

shows the largest variations. The coarsest value also is unable to reach the maximum lift in comparison to the other parameter values. Overall, it appears that the reference mesh value is a sufficient best-practice value. The finer solutions only differ from the reference solution in the integrated forces and moments by a few tens of counts.

C. Variations in Global Max Spacing

Table 8 shows the point growth as the max global spacing for the near-body grids are varied. There is a larger growth in the point count because decreasing the max spacing on the surface also decreases the spacing on the off-body grids due the best-practices for overset grid generation. The node count and spacing do not follow a direct ratio, however. While decreasing the spacing increases the node count in both directions for off-body grids and in the tangential direction for conforming grids, the mesh growth in the normal direction for conforming grids is decreased since the grid does not need to grow as far to reach a lower max global spacing in the outer boundary. Figure 22 shows the pressure and

Table 8 Node count with variations in global max spacing.

Δs_{max}	$1.0\%c_{ref}$	$1.33\%c_{ref}$	$2.0\%c_{ref}$	$3.0\%c_{ref}$	$4.5\%c_{ref}$
Node Count	868168	559364	333566	231795	187653

skin-friction coefficients for variations in the maximum global spacing. The force distributions across the sections exhibit relatively small variations across the parameter range. Some slight changes in the separation location can be observed in the skin-friction of the flap element. Figure 14d also shows a traversal range of approximately 1% for the flap separation point. The stagnation points in Figure 14 show much smaller variations, which correlate with the variations observed in the pressure coefficients.

Like the variations in the leading-edge spacing, the lift variation for the max surface spacing varies across a range of approximately one hundred counts. Figure 15 shows that the major contributor of the variations occurs in the main element, since the other elements only vary by approximately 10 counts. Overall, this corresponds to a 0.3% variation range across all elements, and the variation pattern is consistent across all three elements.

Figure 16 shows that the total drag only varies over a range of approximately five counts. The main element exhibits a variation of a few counts, while the slat and flap exhibit a variation of approximately fifteen counts with an opposing variation pattern. Figure 18 and 19 shows that the variations in the drag are related to pressure effects. Figure 17 shows that the moment coefficients exhibit a similar variation pattern to the lift across the full configuration and the individual elements.

Varying the global max spacing affects the growth distance of the conformal meshes as well as the resolution of the wake block. Decreasing the max spacing reduces the mesh growth distance, which also increases the number of active

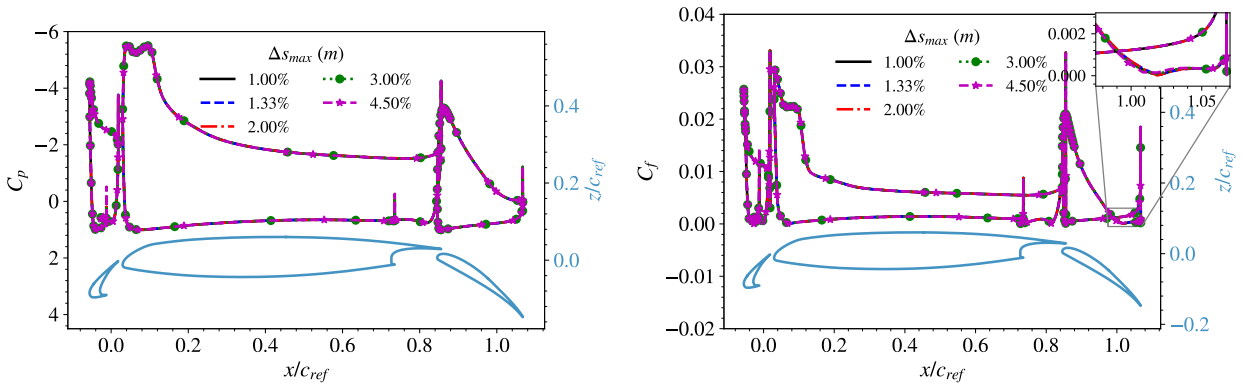

(a) **(b)**

Fig. 22 (a) Section pressure and (b) skin-friction coefficients for variations in max global spacing.

off-body points closer to the walls. This may be introducing more points in the suction regions of each element, which can improve the resolution of the total circulation in the flow and result in the lift variation that is shown in Figure 15. The resolution of the wake block is also refined as the global max spacing is decreased. This can improve the resolution of the momentum loss in the wake, which may be the cause of the lift and drag behavior at the two finest spacings.

Figure 23 shows the lift and drag polars for the variations in the max surface spacing. Because the variations are small to begin with in the reference case, the polars do not show significant discrepancies between the solutions in the linear region of the lift. However, in capturing $C_{l,max}$, some slight discrepancies can be observed. The largest spacing, $\Delta s_{max} = 0.045$, achieves a lift that is much higher than the other solutions. The fact that the solutions only vary approximately 1% or less in all force and moment coefficients indicates that a max surface spacing of 3% of reference chord may be a reasonable choice for a best practice mesh.

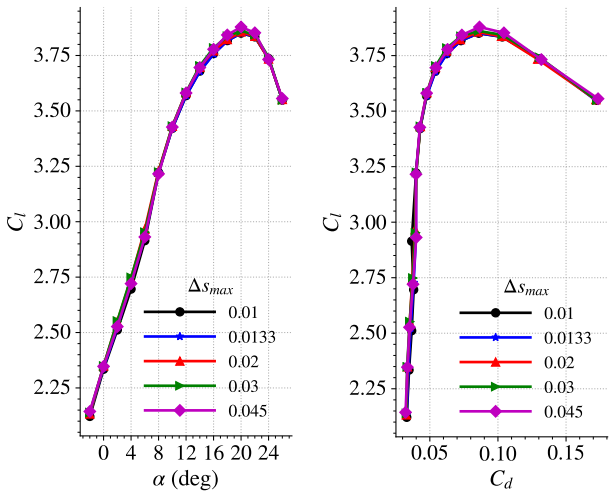

(a) **(b)**

Fig. 23 (a) Lift curves and (b) drag polars varied with global max spacing.

D. Variation of Stretching Ratio

Table 9 shows how the node count varies as the stretching ratio is changed. The node count growth associated with a smaller stretching ratio is expected since more points are needed to stretch the edge-lengths to the max surface spacing in the conformal grids. For these meshes, the stretching ratio is the same in the normal and tangential direction, so the point count increases in both directions. Likewise, the wake grids for each element also undergo the same refinement in the normal and tangential directions. Figure 24 shows the result of varying the stretching ratio on the meshes. The mesh is finer as it transitions to the shear layer spacing and also away from the shear layer spacing. The overlap between the conformal and off-body meshes occur much further away from the wall surface.

Table 9 Node count with variations in stretching ratio.

Stretching Ratio	1.05	1.1	1.15	1.2	1.3	1.4
Node Count	555055	325223	262209	231795	205687	194567

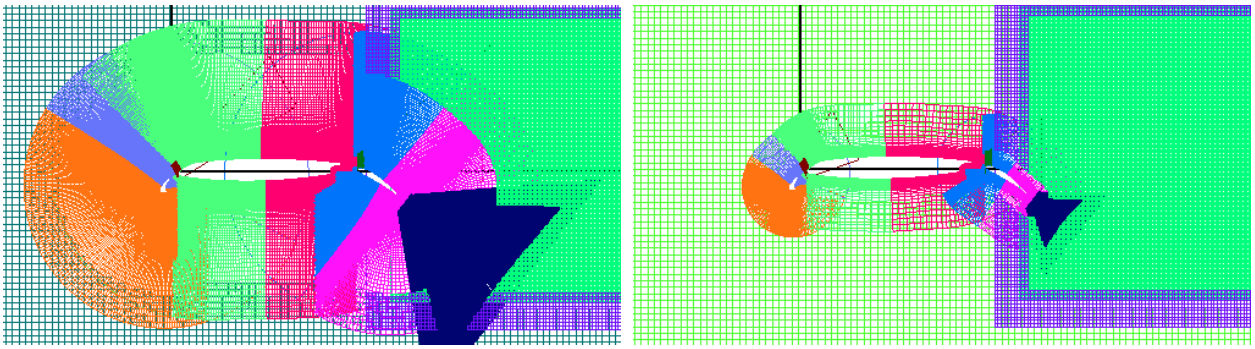

(a) SR = 1.05 **(b) SR = 1.3**

Fig. 24 Grid generated with (a) stretching ratio of 1.05 and (b) stretching ratio of 1.2.

Figure 25 shows the pressure and skin-friction coefficient distributions as it varies with the stretching ratio. In the pressure coefficient distribution, the majority of discrepancies can be observed across the upper surfaces of each element. The zoom shows that the pressure on the upper surface decreases with the stretching ratio, and the stretching ratios higher than the standard 1.2 exhibit larger discrepancies amongst the solutions than the remaining solutions with a stretching ratio of 1.2 or lower. The bottom surface appears to not be as sensitive to the variation of the stretching ratio. The skin-friction coefficient shows a similar story on its upper surface. The skin-friction distribution appears to decrease with the stretching ratio. Again, the stretching ratios greater than 1.2 exhibit a larger variance in the results, especially with regards to the separation location. The higher stretching ratios predict earlier separation than the other solutions.

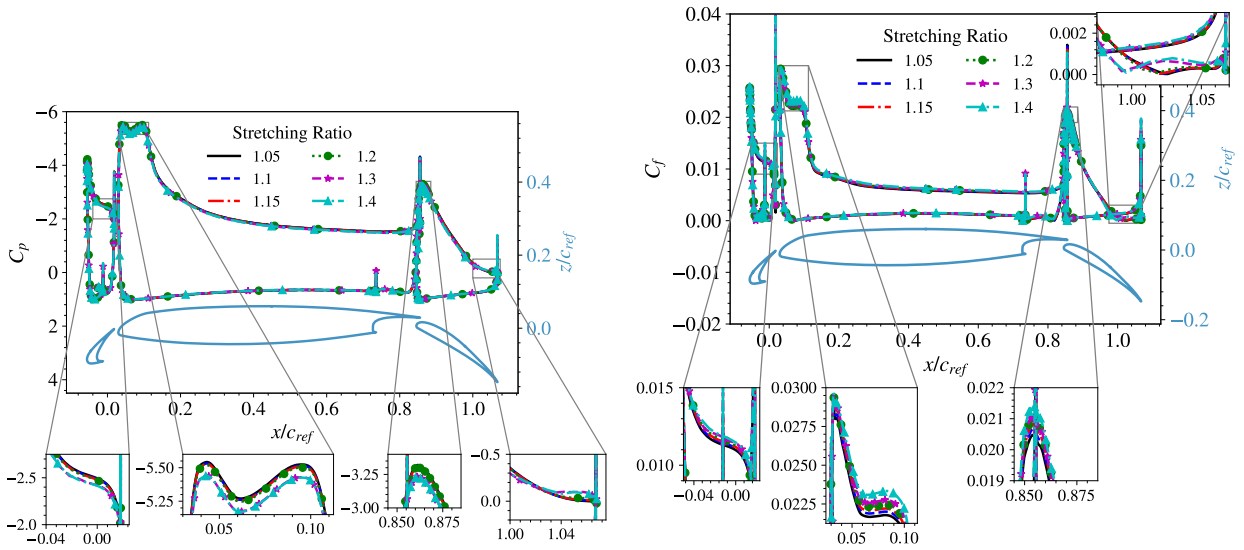

(a) **(b)**

Fig. 25 (a) Section pressure and (b) skin-friction coefficients for variations in stretching ratio.

Figure 14 shows the slat and flap stagnation points traversing aft-ward as the stretching ratio decreases. The stagnation points in the main element do not vary as much with the stretching ratio. Figure 14d also shows the aft-ward traversal of the separation point. These trends indicate an increase in lift and decrease in drag, which implicates that reducing the stretching ratio improved the upstream momentum resolution, and thus the lift circulation throughout the grid.

The lift variation against the stretching ratio is consistent for all elements and full configuration in Figure 15. There is a steady increase in the lift when the stretching ratio is reduced below 1.2, while the lift is drastically reduced when the grid is stretched at a growth rate of 1.3 or higher. Overall, the variation in lift of the full configuration covers a range of nearly 800 counts in lift. However, for a stretching ratio of 1.2 or below, the lift varies across approximately 160

counts in lift. For the same stretching ratios, the variations in the slat and flap covers a range of approximately 20 counts, while the range for the main element covers approximately 120 counts.

This trend is likely due to the improved resolution of the suction regions of reach element. The smaller stretching ratios allow the near-body meshes to grow further away from the wall. Because of this, more of the suction regions of each element can be resolved by the leading edge spacing, which can improve the circulation resolution. Additionally, a lower stretching ratio also increases the local resolution in the normal direction, which can improve the capturing of the extrema of the tangential velocity in the normal direction near the body. A larger stretching ratio, on the other hand, results in a shorter growth distance since the global max spacing is reached at a shorter distance. This results in part of the suction regions to be resolved by the off-body mesh spacing, which can reduce the quality of the lift circulation in the solution. A stretching ratio larger than 1.2 can also introduce discretization errors that can reduce the order of accuracy of the scheme.

The effect on the circulation can also be seen in the drag variation in Figure 16. As expected, the drag decreases with the increase of the lift. The slat shows a range of approximately 100 counts of drag, while the flap shows a varying range of approximately 80 counts drag. The main element only shows variation over a range of 10 counts of drag.

A variation similar to that of the lift can be observed in the pitching moment coefficient in Figure 17. The overall decreasing moment coefficient is indicative of increased lift due to the circulation. The slat and main element vary over a range of tens of counts, while the flap varies the most with nearly 100 counts.

A further examination of the pressure and viscous drag in Figures 18 and 19 indicate that, like the other variables, the pressure drag is the major contributor to the variations present in the total drag. Overall, the total drag varies in a similar manner to the pressure drag. It is interesting to observe that, while the viscous drag variation is small for all variables investigated, stretching ratio shows the most variation. While the other investigated parameters only exhibit variations of less than a count for the viscous drag, the stretching ratio exhibits a variation of a few counts. The largest contributor to the variations is in the main element, while the slat and flap elements vary less than a single count. For the slat and main elements, the viscous drag varies nearly linearly with the stretching ratio. The flap, however, does not have a clear relationship between the variation with the stretching ratio. Of the parameters examined, only the stretching ratio affects the grid spacings very close to the wall since the stretching occurs in the next grid spacing after the initial wall spacing. It is possible that the stretching has an effect on the numerical approximation of the shear stress near the wall, resulting in the observed trend.

Figure 26a and 26b shows the lift and drag polars as they vary with the stretching ratio. Slight discrepancies occur in the linear region of the lift polar. The discrepancies increase as the solutions compute the $C_{l,max}$. The higher stretching ratios predict a higher maximum lift in comparison to the max lift predictions of stretching ratios at 1.2 or less. Since the meshes at a lower stretching ratio exhibit much finer spacing, it may be reasonable to assume that the solutions from the lower stretching ratios are closer to the proper answer.

E. Variation in Shear-Layer Spacing

Table 10 shows the node count as it varies with the spacing in the shear-layer region. The growth of the points is relatively moderate since the clustering only occurs some short distance away in the normal direction to the wall.

Table 10 Node count with variations in shear-layer spacing.

Shear-Layer Spacing	25	50	100	200	400
Node Count	450917	304893	231795	194765	177089

Figure 27 show the surface pressure and skin-friction coefficients of the configuration. Overall the pressure coefficients show some minor discrepancies on the upper surface. The skin-friction, on the other hand, shows some moderate variation on the upper surface of the flap, indicating differences in flow separation prediction. The zoom in Figure 27b shows that the mesh with the largest spacing is the only out-lier solution, while the other meshes shows some agreement in the separation point location. These observations are corroborated by the locations of the stagnation and separation points in Figure 14.

The lift coefficient shows a variation over a range of approximately 200 counts for the full configuration in Figure 15. The main element exhibits the largest range of variation, while the slat and flap vary approximately twenty counts each. Across all elements, the lift variation takes on a consistent pattern. The lift exhibits small increases as the spacing gets finer in the coarser end of the parameter space, and much larger increases with refinement in the finer end of the

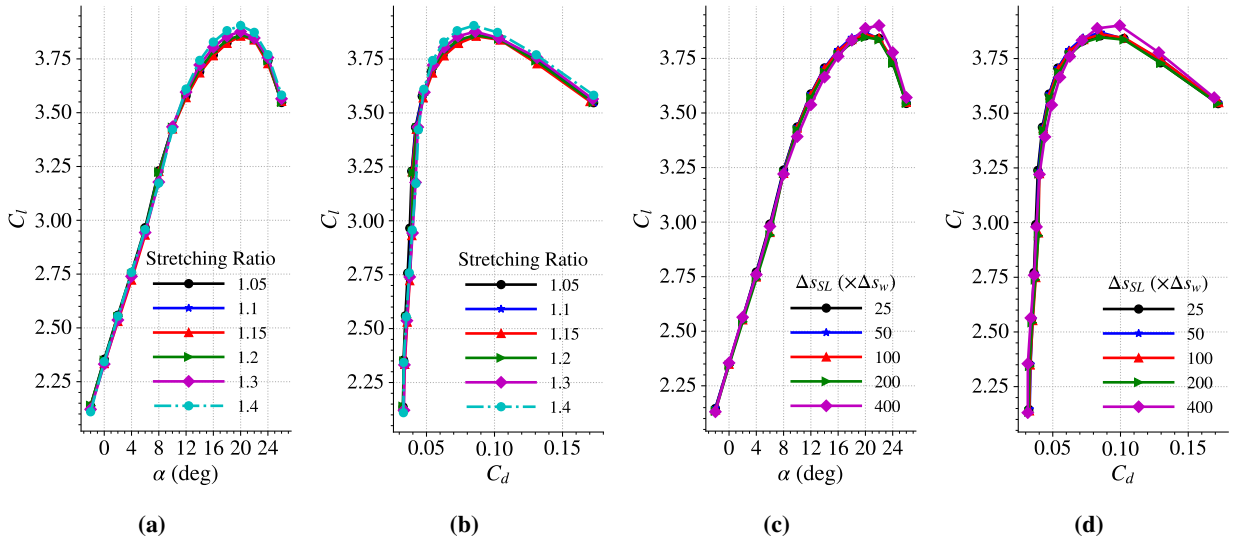

Fig. 26 Lift curves and drag polars for variations in stretching ratio ((a) and (b)) and shear layer resolution ((c) and (d)).

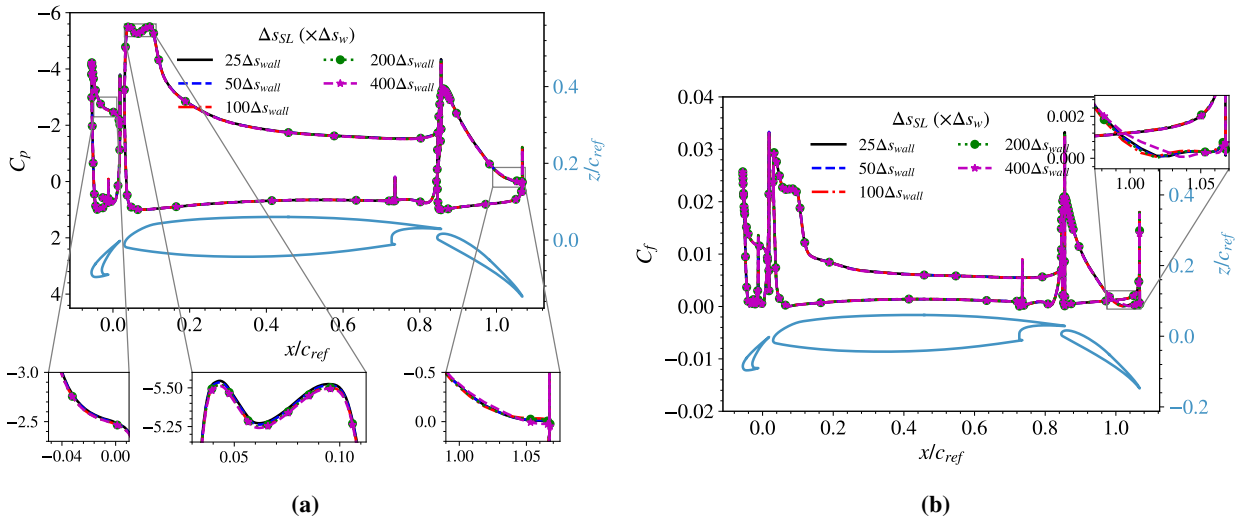

Fig. 27 (a) Section pressure and (b) skin-friction coefficients for variations in stretching ratio.

spectrum. It is likely that refining the spacing has an inadvertent effect of improving the resolution in the suction regions of each element.

Figure 16 supports this argument because, for the same finer spacing, there is a ten count drop in the full configuration drag where one would expect an increase in drag due to improved resolution of the momentum loss. Figure 16b shows almost no variation in the coarser spacings, followed by a thirty count drop in drag as the spacing becomes finer than that of the reference mesh. Normally, it is expected that the drag would *increase* since there is improved resolution of the wake. Furthermore, consider the fact that refining this part of the grid in the slat simultaneously refines the suction region and the cove region, which both can contribute to the decrease in drag. Figure 16d shows a similar effect in that improving the resolution in the suction region results in a net increase in drag for the flap. On the other hand, Figure 16c shows that the main element only varies a few counts of drag, indicating lack of sensitivity of the solution to the shear layer spacing. It is likely that the coarsest spacing is already relatively fine for the wake of the main element, and that additional refinement only has marginal effects on the computation of drag due to the wake. Figure 18 and 19 also show

that the major contributor to the variations come from the pressure drag, indicating that the change in drag is due to the resulting change in how the circulation is captured in the solution. Figure 17 also shows a similar effect on the moment coefficient due to a changes in the lifting circulation.

Figure 26c and 26d shows the lift and drag polars as it varies with the shear layer spacing. Like the other parameters, the coarsest spacing shows the largest discrepancies, while the other solutions are closer together. The coarsest mesh overpredicts the $C_{l,max}$ and slightly underpredicts the corresponding drag. There is more agreement across the parameter space in the linear region of the lift curve.

Overall, it seems that using a spacing of 100 times the wall spacing is reasonably sufficient for resolving the wake of an upstream element. It is interesting to observe the unintended effect that refining the shear-layer spacing has on the circulation of flow. The effect is similar to varying the stretching ratio in the normal direction.

F. Best-Practice Mesh and Grid Convergence Study

Table 11 shows the selected parameters for the best-practice mesh. Most selections are similar to the reference mesh, except for the stretching ratio. The max leading-edge turning angle and the max surface spacing are selected from the reference mesh since the solutions do not vary as significantly with the refinement. The shear layer spacing of the reference mesh is also selected since it appears that it is sufficient in performing its task of resolving the wake resolution of an upstream element.

Table 11 Best-practice selection for each mesh parameter.

Mesh Parameter	$n_{p,TE}$	$\Delta\theta_{LE}$	Δs_{max}	Δs_{SL}	SR
Value	9	1.0°	$0.03c_{ref}$	$100\Delta s_w$	1.15

For the trailing-edge resolution, the value for the reference mesh is also selected. On the basis of the drag, nine points appears to be sufficient to capture the total drag since increasing the resolution provides no realize-able improvements to the total drag. This is also the case for the main element. It is interesting to observe the effect on the slat and flap elements, however, since the variation of the drag beyond a resolution of nine points appear to be opposite and nearly equal in magnitude. Thus, the drag is independent of the trailing-edge resolution beyond a nine-point resolution. On the basis of lift, nine points appears to provide the maximum obtainable lift for the mesh. Increasing the resolution may be introducing additional smaller length-scale phenomena that is not equivalently resolved at other locations of the mesh. Additionally, variation of other parameters indicate that the circulation in the solution may not yet be fully resolved, and so it may not be reasonable or accurate to introduce additional damping through the momentum loss in the trailing edge resolution.

Table 12 Mesh parameter settings for each grid refinement, SR = 1.15 (best-practice mesh bolded).

Refinement Level	**L1**	**L2**	**L3**	**L4**
$n_{p,TE}$	5	**9**	17	33
$\Delta\theta_{LE}$ (deg)	2.0	**1.0**	0.5	0.25
Δs_{max} ($\times c_{ref}$)	0.06	**0.03**	0.015	0.0075
Δs_{SL} ($\times\Delta s_w$)	200	**100**	50	25
Δs_{wgTE} ($\times\Delta s_w$)	10	**5**	2.5	1.25
Node Count	129980	**262209**	686587	2166259

Finally, a smaller stretching ratio of 1.15 is selected for the best practice mesh. Varying the stretching ratio and the shear-layer spacing revealed that it is possible that the overall circulation due to lift is still somewhat under-resolved with the reference mesh, and that these two mesh parameters increased the resolution of the physical features that contribute to the circulation like the suction regions. Thus, it may be prudent to start a grid-convergence analysis with a mesh that is able to capture most of the circulation.

Table 12 outlines the mesh parameters used to perform the grid convergence study. The study is performed by refining each parameter by a factor of two for each successive level. Figure 28 shows the grid convergence analysis of the solution computed at $\alpha = 8°$. The best-practice mesh exhibits less than a percent difference in the lift and moment

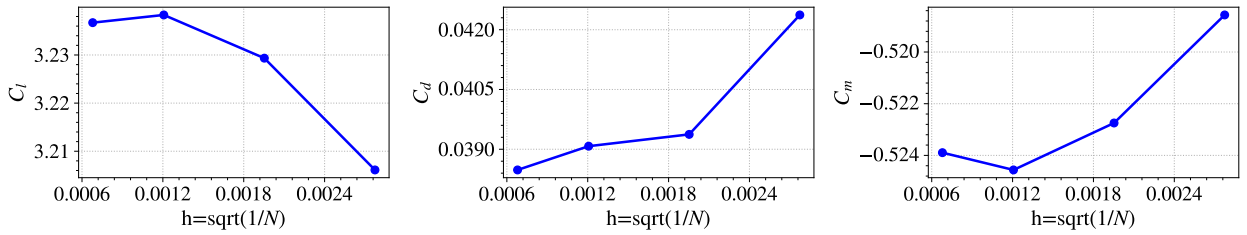

Fig. 28 Convergence of force and moment coefficients for full configuration at $\alpha = 8°$ (best practice mesh is $h = 0.0020$).

coefficient and approximately an 8 count difference in drag. Figure 29 shows the grid convergence for $\alpha = 16°$. Like the 8 degree case, the lift and moment coefficients show a discrepancy of less than a percent. However, the drag coefficient of the best practice mesh differs from the finest solution by approximately twenty counts. Overall, the results show that the solutions do asymptotically approach a particular result.

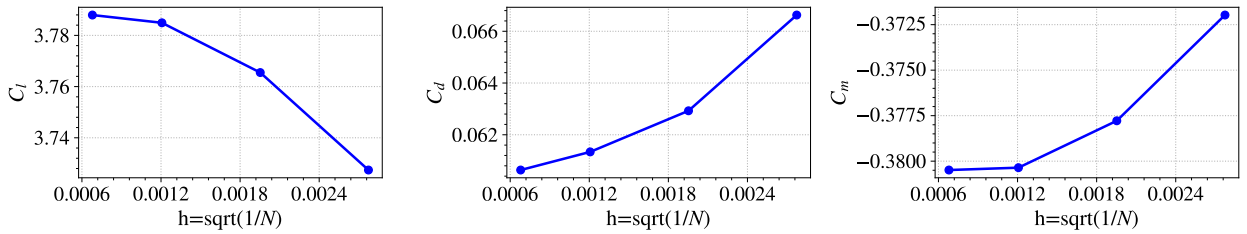

Fig. 29 Convergence of force and moment coefficients for full configuration at $\alpha = 16°$ (best practice mesh is $h = 0.0020$).

Figure 30 shows the velocity contours of the two grid converged cases on the finest grid. Figure 30a shows the solution at an angle-of-attack of 8 degrees. The slat and main elements shed a thin wake layer over the subsequent elements. A small separation region can be observed near the trailing edge of the flap, as well as the deceleration of the main-element wake behind the flap. The solution at 16 degrees in Figure 30b shows that the deceleration region now completely encompasses the region aft of the flap along the chord line, while the separation region is now reduced to a thin wake near the trailing edge of the flap. Between the flap and the deceleration region there is a slightly higher-speed flow region. The upper surface of the slat and main elements exhibit similar features as the 8 degrees solution, while the cove region of the slat no longer exhibits a shear layer developing in the region.

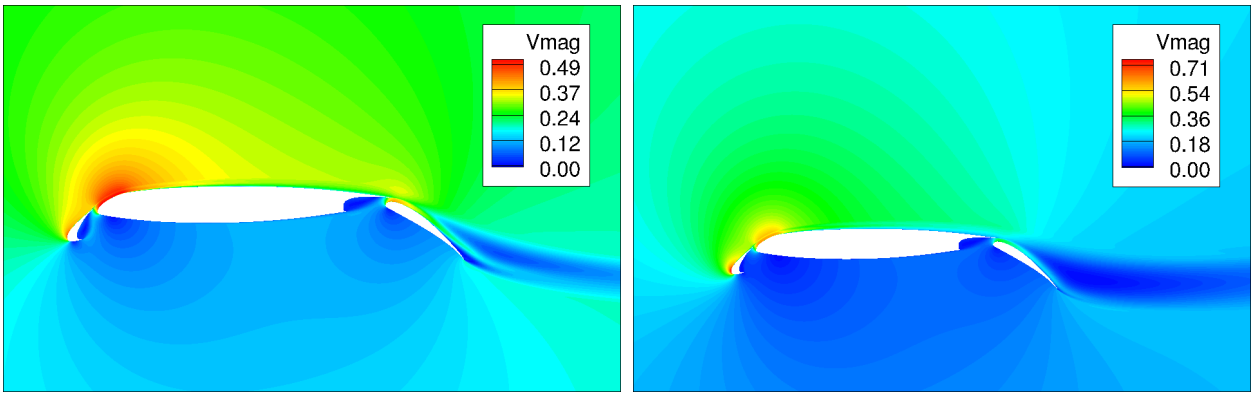

(a) $\alpha = 8°$ **(b)** $\alpha = 16°$

Fig. 30 Velocity magnitude contours around configuration.

VI. Adaption Study Results

Adaption is applied to a solution from a coarse mesh to investigate the minimum quality for a mesh. Table 13 details the mesh parameters to generate the mesh. Most of the parameters come from the coarser values in the mesh parameter study. The stretching ratio and the wall spacing is kept the same as the reference mesh, however. The shear-layer refinement region and the O mesh wake grids are not included in the mesh.

Table 13 Mesh parameters used to generate coarse mesh.

Mesh Parameter	Δs_w	$n_{p,TE}$	$\Delta\theta_{LE}$	Δs_{max}	Δs_{SL}	SR
Value	$4.323 \times 10^{-6}\ c_{ref}$	3	2.0°	$0.045 c_{ref}$	N/A	1.2

The resulting mesh with the minimum hole-cut for geometry exhibited difficulties in reaching a converged solution with adaption. Removing the excessive overlap appeared to alleviate the issue. Figure 31a shows the resulting initial coarse mesh with additional simple cutting procedures for removing excess overlap. This mesh is meant to be representative of a meshes generated without much a prior knowledge of the flow. For instance, this may be a mesh that is generated from an automatic mesh generation process. Thus, aside from the boundary layer, no special attention is paid to refining any particular region.

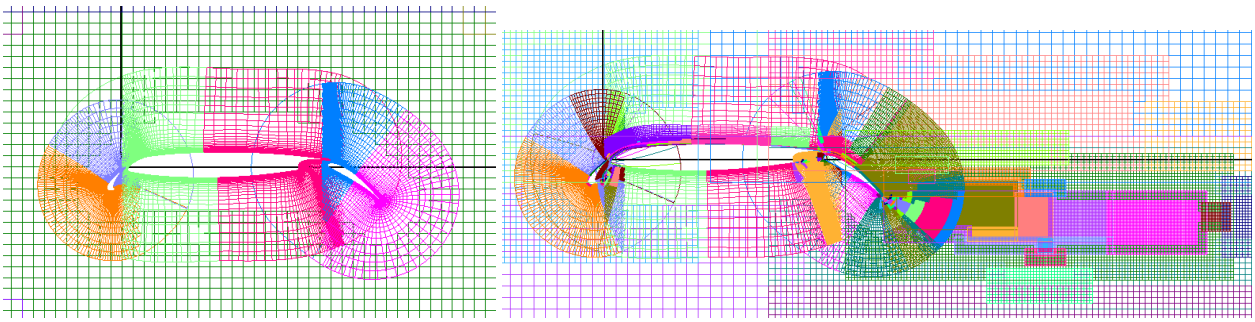

(a) **(b)**

Fig. 31 (a) Initial mesh. (b) The final adaptive mesh with four levels of refinement at $\alpha = 8°$.

Three maximum allowable levels of refinement are investigated. Table 14 shows the point-count growth as the solution is allowed to refine to the specified level. To reduce the use of computational resources, the refinement is limited to region a two chord distances away from the away from the geometry. Figure 31b shows the final mesh where the OVERFLOW applied the refinement. The adaption appears to be focused between adapting the near-body flow features and resolving the wake off the trailing edge of each element.

Table 14 Node count with variations in maximum allowable levels of refinement.

Max Allowed Refinement Level	No Refinement	2	3	4
Node Count	56102	318296	519821	962668

Figure 32 and Figure 33 provide a closer examination of where the adaption is applied in the grid. As expected, the grids shows that the adaption is concentrated in regions of sharp gradients. This includes the shear layers from the wake of each element and the shear layers in the cove regions. The main-element wake deceleration region behind the flap and flap separation region is also refined. Some refinement is also applied to the suction regions of each element, but to a lesser extent. This is also expected since the velocity gradients in that region are not particularly sharp.

Figures 34, 35, and 36 show the force and moment coefficients for a solution computed with a specified maximum allowed level of refinement for adaption. The finest solution from the grid convergence study is also included for comparison. In the total lift, there is a nearly forty count discrepancy between the lift of the fine solution and the finest adaptive solution. Most of the discrepancy is concentrated in the main element, while the slat and flap only vary a few counts.

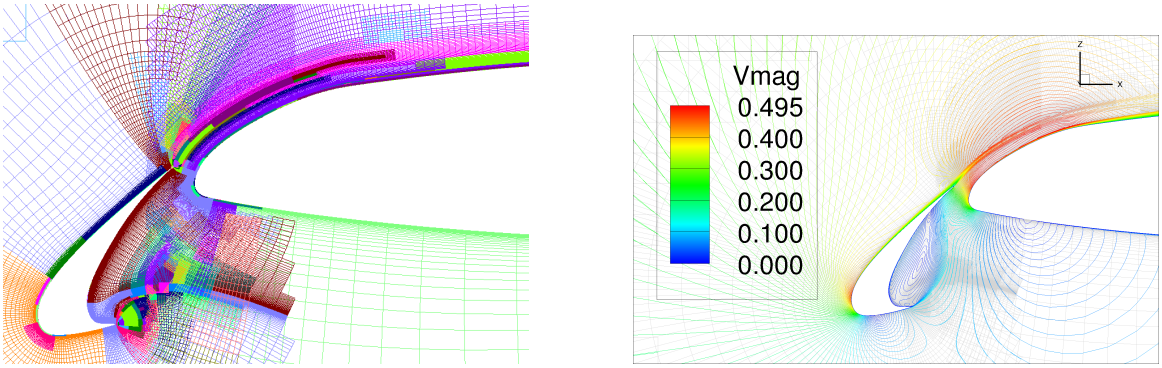

(a) (b)

Fig. 32 Refinement regions in the slat at four levels of refinement, $\alpha = 8°$. (a) Mesh. (b). Contours of velocity magnitude.

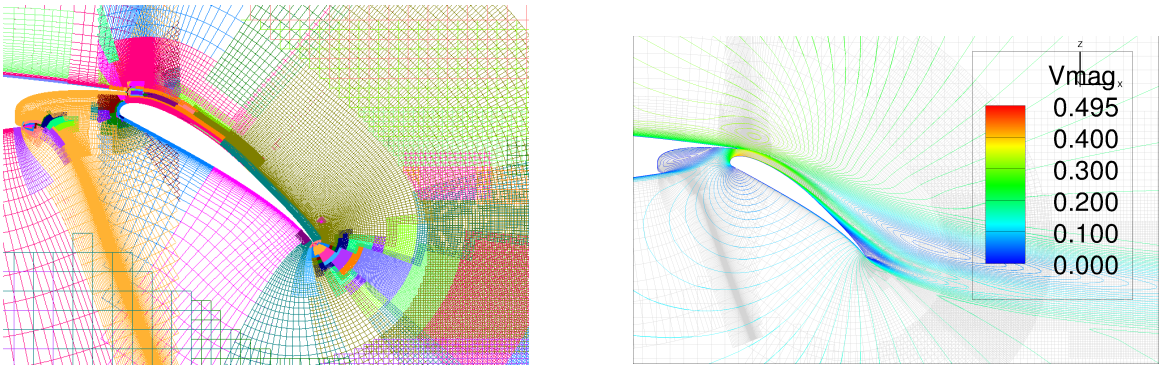

(a) (b)

Fig. 33 Refinement regions in the flap at four levels of refinement, $\alpha = 8°$. (a) Mesh. (b). Contours of velocity magnitude.

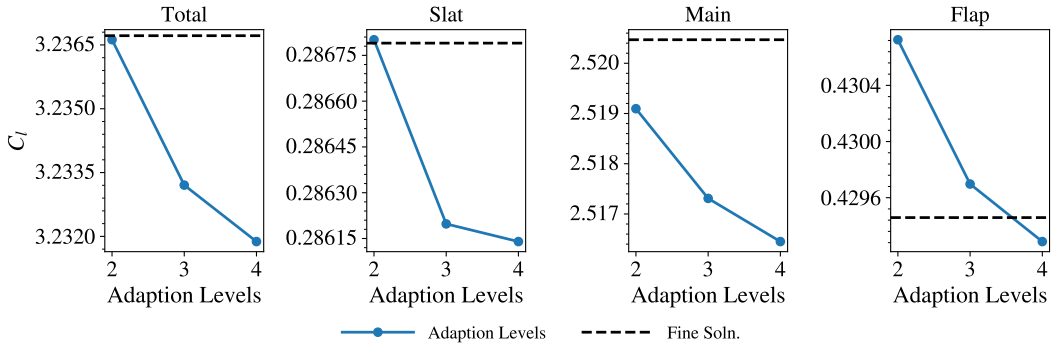

Fig. 34 Lift coefficient trends with levels of adaption, $\alpha = 8°$.

In the drag, there is a discrepancy of nearly twenty counts. This difference appears to be evenly split in the slat and the main element, while the flap shows negligible discrepancies. Most of the discrepancy is accounted for the in the pressure drag, while the viscous drag exhibits a discrepancy of approximately 2 counts. In the moment coefficient, the finest resolutions show reasonable agreement. There are only a few counts of discrepancy across all the elements. Figure 37 shows the force and moment coefficient trends with adaption levels at $\alpha = 16°$. The discrepancy is much greater here than at the lower angle of attack. Figure 38 shows the stagnation and separation points for the two angles of attack.

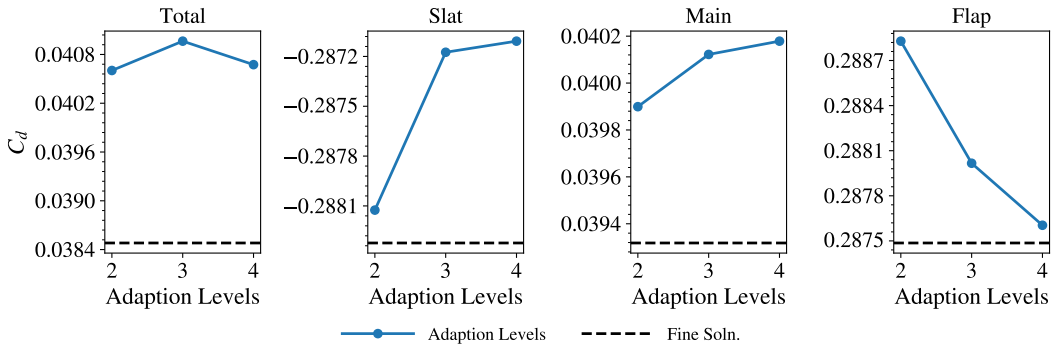

Fig. 35 Drag coefficient trends with levels of adaption, $\alpha = 8°$.

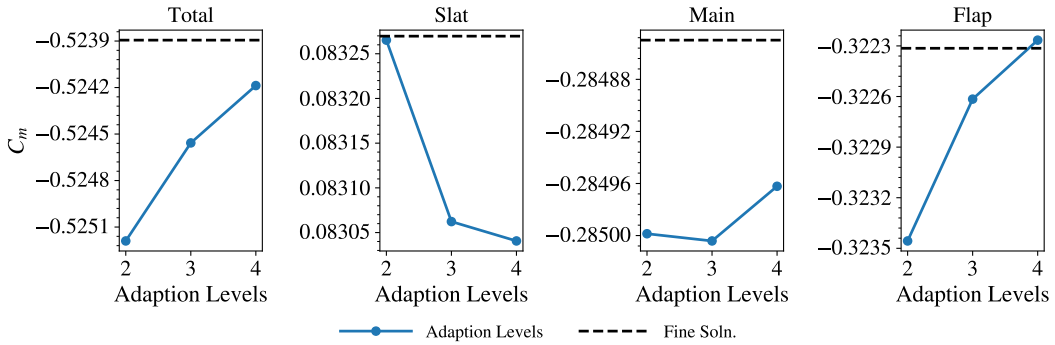

Fig. 36 Moment coefficient trends with levels of adaption, $\alpha = 8°$.

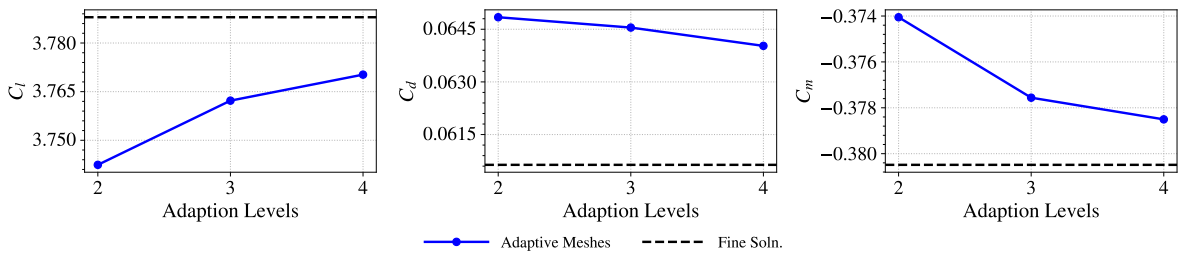

Fig. 37 Total force and moment coefficient trends with levels of adaption at $\alpha = 16°$.

The discrepancies between the solutions can likely be attributed to the adaption strategy. Certain important regions that do not exhibit large or sharp gradients, such as the suction regions in the leading edge, are not targeted for adaption. Consider Figure 39, which shows the mesh at the leading edge of the slat for the coarse starting grid, the grid with four levels of adaption, and the level three refinement grid from the grid-convergence study. Most of the slat leading edge away from the boundary layer region is similar to the initial coarse mesh. Much of the refinement occurs near the wall where the adaption sensor is targeting the sharp gradients in the boundary layer. Comparatively, the level three mesh has a finer resolution away from the wall in the normal and tangential directions. However, in other regions where refinement occurs, such as in the wake regions or shear layers, the adaption strategy is similar to the a prior knowledge used to the cluster points in the baseline mesh.

Figure 40 shows the pressure coefficient distributions for each element in the configuration. Amongst the adaption levels, the results show reasonable agreement with each other. In comparison with the grid-converged solution, the discrepancies are small for the $\alpha = 8°$ case. The grid-converged solution shows lower pressures at the suction region and in the separation region at the flap. However, in the case of $\alpha = 16°$, there is a discrepancies at the suction peaks of the main and flap elements. Figure 41 shows the lift and drag polars for each maximum refinement level. Overall the max lift coefficient is comparatively lower than the typical max lift coefficients observed in the mesh parameter

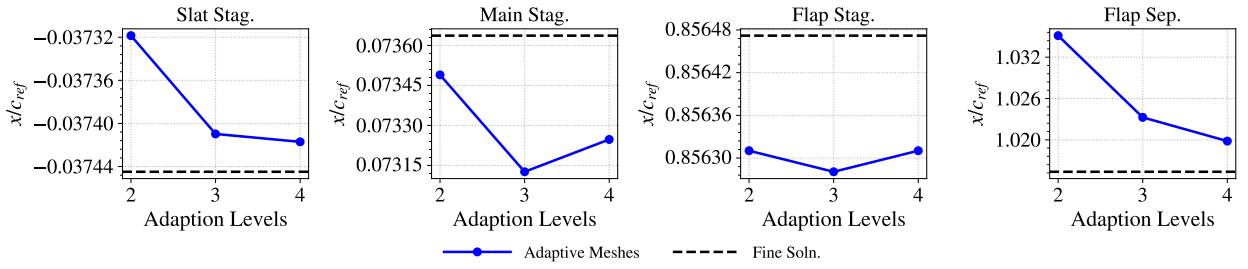

(a) $\alpha = 8°$

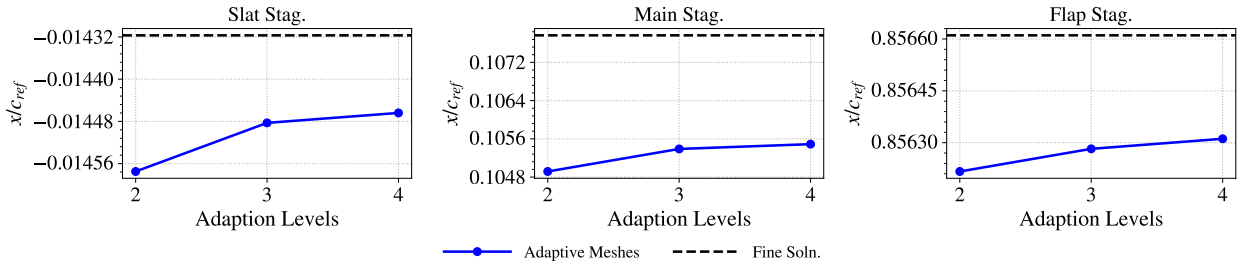

(b) $\alpha = 16°$

Fig. 38 Stagnation and flow separation locations at $\alpha = 8°$ and $\alpha = 16°$.

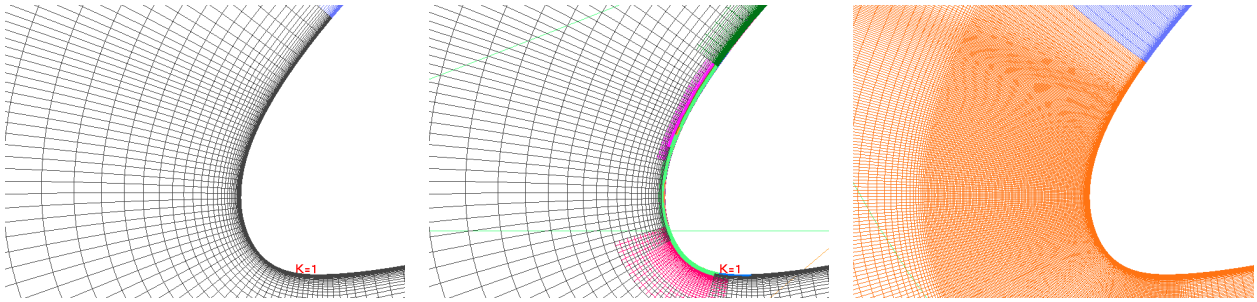

(a) **(b)** **(c)**

Fig. 39 Mesh at slat leading edge for the (a) initial coarse mesh, (b) the adaptive mesh with four levels of refinement, and (c) the level 3 mesh from the grid-convergence study.

variation. The finest adaptive mesh exhibits a $C_{l,max}$ of 3.8486, while the solutions from the mesh parameter variation tend to vary around 3.8600.

VII. Summary

A mesh parameter study was performed to investigate the effects of the parameter variation on the solution for a multi-element configuration in a structured overset framework. The varied parameters consist of the max surface spacing, trailing edge resolution, leading edge resolution, shear-layer spacing, and stretching ratio. The parameter variations were performed on a baseline overset mesh with O mesh topology for the near-body grids. A priori refinement was also included in the mesh in regions where wakes and shear layers are expected to develop. A wake grid is also added to each O mesh to provide a similar resolution to a C mesh.

The results revealed that the solution exhibits sensitivities to the discretization of the suction regions and of the wakes of each element. The stretching ratio, trailing edge resolution, and shear-layer spacing exhibited some of the largest variations in the solution with the parameter variations. The stretching ratio and the shear-layer spacing directly affect the overall normal spacing in the near-body mesh. Reducing the stretching ratio or refining the shear-layer spacing has the effect of increasing the circulation around the configuration, which is evidenced by the increase in lift and

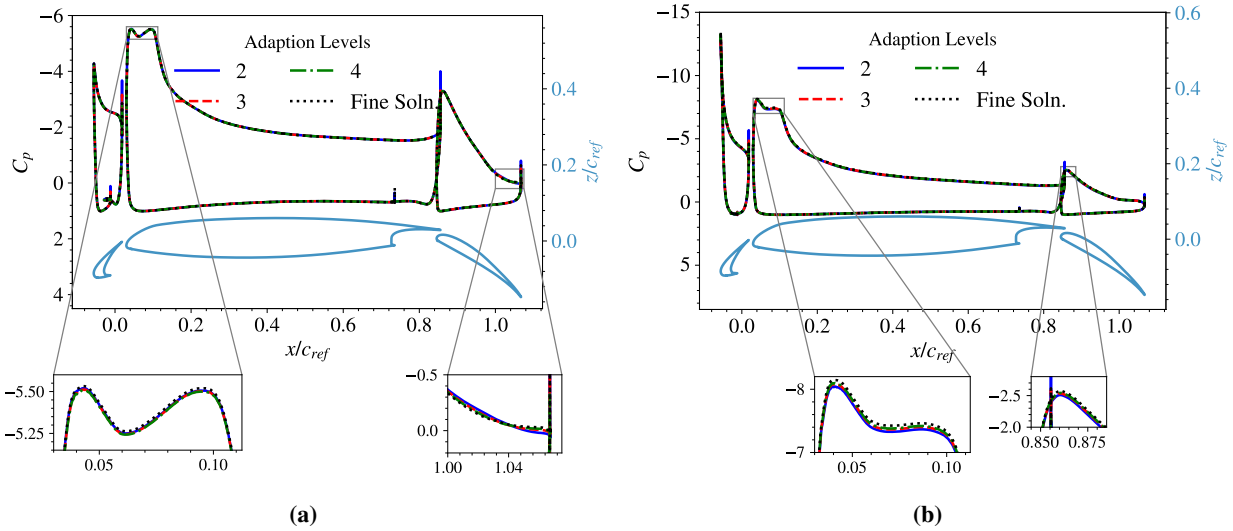

Fig. 40 Section pressure coefficients for each level of adaption at (a) $\alpha = 8°$ and (b) $\alpha = 16°$.

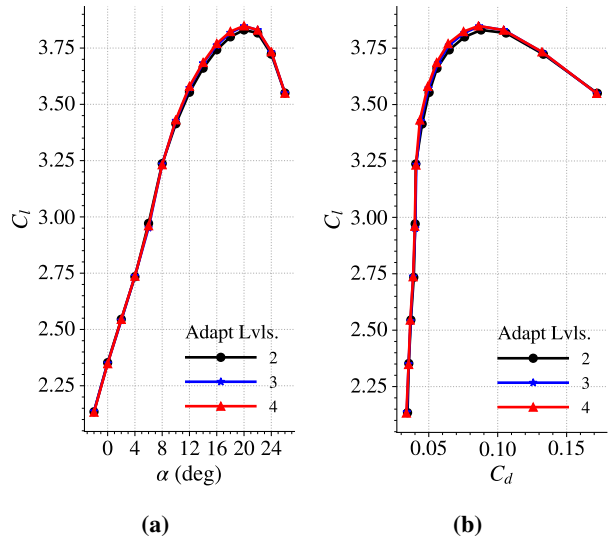

Fig. 41 Lift (a) and drag (b) polars for variations in adaption levels.

decrease in drag. Increasing the trailing edge resolution, however, has the opposite effect. While the overall drag of the configuration does not change very much as the trailing edge is refined, the overall lift does decrease. Refining the trailing edge resolves the momentum loss and appears to have a damping effect on the circulation downstream of a given element. A grid refinement study was then performed with the best-practice mesh based on the mesh parameter variation at an angle of attack at 8 and 16 degrees. In both cases, the best-practice mesh showed convergence with mesh refinement.

A mesh adaption study was also performed to investigate the minimum mesh needed to compute the solution with OVERFLOW's adaption process. The adaption methodology targets sharp gradients in the solution based on the second undivided differences of the conservative variables. Important flow features with sharp gradients, such as the wakes and shear layers, are captured well by the solution through the adaption process. The resulting refinements made by the adaption process substantiates the a priori refinements made in the manually generated meshes for capturing features like wakes. However, because the adaption process is only based on sharp gradients, other locations like the suction regions with smooth flow features are not specifically targeted. This is likely the cause of the discrepancies

between the solutions obtained from adaption and the solution obtained from a consistent mesh refinement. Overall, the feature-based adaption examined in this paper is capable of capturing the flow features, but it is not as effective as a grid refinement study to obtain a grid-independent solution.

VIII. Acknowledgements

This work is partially funded by the following NASA Projects: Transformational Tools, and Technologies (TTT) and Revolutionary Vertical Lift Technology (RVLT). Computational resources have been provided by the NASA Advanced Supercomputing (NAS) facility at NASA Ames Research Center. The authors would like to thank Dr. Thomas Pulliam from NASA Ames Research Center for insightful discussions and advice on using adaptive mesh refinement in OVERFLOW.

References

[1] Vassberg, J. C., Tinoco, E. N., Mani, M., Brodersen, O. P., Eisfeld, B., Wahls, R. A., Morrison, J. H., Zickuhr, T., Laflin, K. R., and Mavriplis, D. J., "Summary of the Third AIAA CFD Drag Prediction Workshop," *Collection of Technical Papers - 45th AIAA Aerospace Sciences Meeting*, Vol. 5, American Institute of Aeronautics and Astronautics, Reston, Virigina, 2007, pp. 3178–3214. https://doi.org/10.2514/6.2007-260, URL http://arc.aiaa.org/doi/10.2514/6.2007-260.

[2] Warren, G. P., Andersont, W. K., Thomas, J. L., and Krist, S. L., "Grid Convergence For Adaptive Methods," *10th Computational Fluid Dynamics Conference, 1991*, 1991. https://doi.org/10.2514/6.1991-1592.

[3] Venditti, D. A., and Darmofal, D. L., "Anisotropic grid adaptation for functional outputs: Application to two-dimensional viscous flows," *Journal of Computational Physics*, Vol. 187, No. 1, 2003, pp. 22–46. https://doi.org/10.1016/S0021-9991(03)00074-3.

[4] "2D CRM-HL Schematic," , 2019. URL http://www.gmgworkshop.com/gmgw25/2D-CRM-HL-Schematic-600x145.png.

[5] Chan, W. M., Gomez, R. J., Rogers, S. E., and Buning, P. G., "Best practices in overset grid generation," *32nd AIAA Fluid Dynamics Conference and Exhibit*, American Institute of Aeronautics and Astronautics, Reston, Virigina, 2002. https://doi.org/10.2514/6.2002-3191, URL http://arc.aiaa.org/doi/10.2514/6.2002-3191.

[6] Chan, W. M., "Best practices on overset structured mesh generation for the high-lift CRM geometry," *AIAA SciTech Forum - 55th AIAA Aerospace Sciences Meeting*, American Institute of Aeronautics and Astronautics, Reston, Virginia, 2017. https://doi.org/10.2514/6.2017-0362, URL http://arc.aiaa.org/doi/10.2514/6.2017-0362.

[7] Chan, W., "Advances in software tools for pre-processing and post-processing of overset grid computations," 2004. URL https://ntrs.nasa.gov/search.jsp?R=20050186738.

[8] Chan, W. M., "Developments in strategies and software tools for overset structured grid generation and connectivity," *20th AIAA Computational Fluid Dynamics Conference 2011*, American Institute of Aeronautics and Astronautics, Reston, Virigina, 2011. https://doi.org/10.2514/6.2011-3051, URL http://arc.aiaa.org/doi/10.2514/6.2011-3051.

[9] Chan, W. M., Chiu, I.-T., and Buning, P. G., "User's Manual for the HYPGEN Hyperbolic Grid Generator and the HGUI Graphical User Interface," Tech. Rep. NASA TM-108791, 1993. URL https://ntrs.nasa.gov/search.jsp?R=19940011311.

[10] Nichols, R. H., Tramel, R. W., and Buning, P. G., "Solver and turbulence model upgrades to OVERFLOW 2 for unsteady and high-speed applications," *Collection of Technical Papers - AIAA Applied Aerodynamics Conference*, Vol. 1, American Institute of Aeronautics and Astronautics, Reston, Virigina, 2006, pp. 91–124. https://doi.org/10.2514/6.2006-2824, URL http://arc.aiaa.org/doi/10.2514/6.2006-2824.

[11] Meakin, R. L., "Object X-rays for cutting holes in composite overset structured grids," *15th AIAA Computational Fluid Dynamics Conference*, 2001. https://doi.org/10.2514/6.2001-2537.

[12] Buning, P. G., and Pulliam, T. H., "Cartesian off-body grid adaption for viscous time-accurate flow simulation," *20th AIAA Computational Fluid Dynamics Conference 2011*, 2011. https://doi.org/10.2514/6.2011-3693.

[13] Buning, P. G., and Pulliam, T. H., "Near-body grid adaption for overset grids," *46th AIAA Fluid Dynamics Conference*, American Institute of Aeronautics and Astronautics Inc, AIAA, 2016. https://doi.org/10.2514/6.2016-3326.

[14] Su, X., "Accurate and robust adaptive mesh refinement for aerodynamic simulation with multi-block structured curvilinear mesh," *International Journal for Numerical Methods in Fluids*, Vol. 77, No. 12, 2015, pp. 747–766. https://doi.org/10.1002/fld.4004, URL http://doi.wiley.com/10.1002/fld.4004.

[15] Langley Research Center, "SA Expected Results - 2D Airfoil Near-Wake," , 2018. URL https://turbmodels.larc.nasa.gov/airfoilwakeverif500c_sa.html.

[16] Langley Research Center, "Turbulence Modeling Resource," , 2020. URL https://turbmodels.larc.nasa.gov/index.html.

[17] Meakin, R. L., "On the spatial and temporal accuracy of overset grid methods for moving body problems," *12th Applied Aerodynamics Conference, 1994*, American Institute of Aeronautics and Astronautics, Reston, Virigina, 1994, pp. 858–871. https://doi.org/10.2514/6.1994-1925, URL http://arc.aiaa.org/doi/10.2514/6.1994-1925.

[18] Vassberg, J. C., DeHaan, M. A., and Sclafani, T. J., "Grid generation requirements for accurate drag predictions based on OVERFLOW calculations," *16th AIAA Computational Fluid Dynamics Conference*, 2003. https://doi.org/10.2514/6.2003-4124.

[19] Noack, R. W., Boger, D. A., Kunz, R. F., and Carrica, P. M., "Suggar++: An improved general overset grid assembly capability," *19th AIAA Computational Fluid Dynamics Conference*, , No. June, 2009, pp. 22–25. https://doi.org/10.2514/6.2009-3992.

[20] Chan, W. M., and Pandya, S. A., "Advances in distance-based hole cuts on overset grids," *22nd AIAA Computational Fluid Dynamics Conference*, American Institute of Aeronautics and Astronautics, Reston, Virginia, 2015. https://doi.org/10.2514/6.2015-3425, URL http://arc.aiaa.org/doi/10.2514/6.2015-3425.

[21] Rogers, S. E., Suhs, N. E., and Dietz, W. E., "PEGASUS 5: An automated preprocessor for overset-grid computational fluid dynamics," *AIAA Journal*, Vol. 41, No. 6, 2003, pp. 1037–1045. https://doi.org/10.2514/2.2070.

[22] Rogers, S. E., "Progress in high-lift aerodynamic calculations," *Journal of Aircraft*, Vol. 31, No. 6, 1994, pp. 1244–1251. https://doi.org/10.2514/3.46642, URL http://arc.aiaa.org/doi/10.2514/3.46642.